CHALMERS
UNIVERSITY OF TECHNOLOGY

# On the use of XFEM for frictional crack face contact

## Application to rolling contact crack growth in rails

Masters's thesis in Applied mechanics

Louise Åkesson

DEPARTMENT OF INDUSTRIAL AND MATERIALS SCIENCE

CHALMERS UNIVERSITY OF TECHNOLOGY
Gothenburg, Sweden 2025
www.chalmers.se

MASTER'S THESIS 2025

# On the use of XFEM for frictional crack face contact

Application to rolling contact crack growth in rails

Louise Åkesson


CHALMERS
UNIVERSITY OF TECHNOLOGY

Department of Industrial and Materials Science
CHALMERS UNIVERSITY OF TECHNOLOGY
Gothenburg, Sweden 2025

On the use of XFEM for frictional crack face contact
Application to rolling contact crack growth in rails
Louise Åkesson



Master's Thesis 2025
Department of Industrial and Materials Science
Chalmers University of Technology
SE-412 96 Gothenburg
Sweden
Telephone +46 (0)31-772 1000

Typeset in LaTeX
Printed by Chalmers Reproservice
Gothenburg, Sweden 1999

On the use of XFEM for frictional crack face contact
Application to rolling contact crack growth in rails
Louise Åkesson
Department of Industrial and Materials Science
Chalmers University of Technology

# Abstract

In this study, an existing numerical framework in 3D for predicting stationary rolling contact fatigue crack growth direction and rate in rails using the eXtended Finite Element Method (XFEM) is extended to account for the influence of crack face friction. To enable this extension, as the first part of the study, the accuracy and robustness of XFEM for stationary frictional cracks in 3D simulations, together with its practical implementation in the commercial FE software ABAQUS, are evaluated through a set of numerical tests. A rectangular block model with a predefined crack geometry is here considered, and the XFEM results in terms of resolved contact shear stresses are compared with the explicitly meshed fracture surface. Crack face friction is implemented using Coulomb's model with varying friction coefficients, and the comparisons are conducted for pure shear load and combined shear–compression load. To account for crack face friction in a stationary setting using XFEM in ABAQUS, crack propagation is suppressed by assigning high critical values for damage initiation and evolution. The trends for the computed shear stresses aligned well those obtained using explicit crack modeling, despite some deviations in absolute values, thereby indicating that the method is sufficiently robust for the qualitative purposes of this study.

As the second part of the study, crack face friction is implemented for pre-existing head check cracks in rails. Crack growth rates and directions are evaluated by employing Paris-type equations and an accumulative vector crack tip displacement criterion, respectively, using stress intensity factors extracted directly from ABAQUS. The results are evaluated for a semi-circular crack plane with two crack radii under a wheel–rail contact load and a combined contact and bending load at three points along the crack front. It was found that crack face friction had a significant impact on growth rates for all points, crack radii and load cases, where a higher coefficient of friction resulted in a lower rate of crack growth. These reductions were found to correspond to large increases in traffic capacity before reaching a certain crack radius. More specifically, the highest investigated friction coefficient was found to reduce growth rates by up to 49% for the case of combined contact and bending loads, which in turn resulted in up to 72% traffic increase for reaching the same crack size, compared to the frictionless case. This highlights the importance of accounting for crack face friction to obtain more realistic predictions and to support efficient maintenance planning of rails. The influence of crack face friction on growth direction was found to be limited, with no clear observed trends due to a limited number of studied cases, under either pure contact or combined contact and bending loads.

Keywords: Frictional contact, Crack face friction, XFEM, Rolling contact fatigue, Crack growth rate, Crack growth direction

# Acknowledgements

I would like to express my gratitude to FS Dynamics for providing the opportunity to carry out this project, and in particular to the FEM group managers, Emina Music and Magnus Ohlson, together with Mohammad Salahi Nezhad, for placing their trust in me from the very beginning.

I am also deeply thankful to my supervisor Mohammad Salahi Nezhad at FS Dynamics and to my supervisor and examiner Fredrik Larsson at Chalmers, whose dedicated guidance, unwavering support, and insightful feedback have been invaluable throughout this project. It has been such an honour to learn and grow under their supervision, and I could not have wished for better mentors.

Louise Åkesson
Gothenburg, September 2025

# List of Acronyms

Below is the list of acronyms that have been used throughout this thesis in alphabetical order:

| | |
|---|---|
| FE | Finite Element |
| FEM | Finite Element Method |
| MGT | Mega Gross Tonnes |
| RCF | Rolling Contact Fatigue |
| SIF | Stress Intensity Factor |
| VCTD | Vector Crack Tip Displacement |
| XFEM | eXtended Finite Element Method |

# Contents

# List of Figures

# List of Tables

# 1 Introduction

This chapter introduces the study by outlining its background and defining its scope. The background and motivation are presented first, followed by the thesis objective and scope and limitations of the study.

## 1.1 Background

The ongoing climate crisis has substantially increased the demand for sustainable living to reduce global greenhouse gas emissions. Statistics from 2016 show that the transport sector accounted for 14% of global greenhouse gas emissions, and was one of the largest consumers of fossil fuels among all sectors (Bergman et al., 2016). However, railways offer a low carbon footprint per passenger-kilometer and tonne-kilometer compared to other modes of transport (Doll et al., 2020), and are also the only widely electrified mode of transport (International Energy Agency (IEA), 2019). Furthermore, they are highly time-efficient and one of the safest modes of transport (Statens institut för kommunikationsanalys (SIKA), 2009). However, both punctuality and safety rely heavily on proper maintenance of the infrastructure due to limited flexibility in railways. Hence, it is of utmost importance to facilitate the continuous expansion of railway infrastructure, and developing reliable numerical models for optimizing maintenance procedures would be instrumental in achieving this.

Crack growth caused by Rolling Contact Fatigue (RCF) is one of the primary factors for deterioration of rails (V. Krishna et al., 2021), which is also highly expensive to mitigate (Zerbst et al., 2009). In addition, it can cause a rail break depending on the depth and size of the crack, where relatively deep and long cracks are typically more prone to deviate to transverse growth and can thus pose a clear safety hazard. Another complicating factor is that RCF cracks mainly grow due to cyclic exposure to high shear and compressive stresses in the wheel–rail contact. The shear can also be affected by tractive stresses caused by accelerating, braking and negotiating curves (Salahi Nezhad, 2024). Thus, RCF cracks grow under complex conditions of non-proportional mixed-mode and compressive loading, resulting primarily from the wheel–rail contact load and its interplay with other present loads in rails. Such loads, among other things, include bending of the rail, and restricted contractions in continuosly welded rails due to ambient temperature variations. Given this complexity, many of the existing fatigue crack growth criteria fail under such conditions, which makes growth rate and direction of RCF cracks challenging to predict (Ekberg and Kabo, 2005). This issue leads to significant uncertainties in predicting crack propagation, particularly under different operational scenarios. One of the most common types of RCF cracks in railways are head checks (P.B.J. Dollevoet, 2010), which are small, inclined surface cracks that typically appear at the gauge corner of the rail head.

Several 2D models exist in the literature to predict RCF crack growth. However, since the wheel–rail contact load has a large influence on the predictions (Salahi Nezhad et al., 2023) and is intrinsically a 3D load, 3D modeling is necessary for more realistic predictions. To this aim, a numerical framework in 3D for predicting RCF crack growth under operational loading has recently been developed in the literature (Salahi Nezhad et al., 2024), using the eXtended Finite Element Method (XFEM) and ABAQUS (Dassault Sys-

tèmes Simulia Corp., 2023a) as the Finite Element (FE) solver. In this framework, head checks are investigated, and modeled as stationary with frictionless crack faces.

The assumption of frictionless crack faces limits the prediction capabilities since crack face friction can have a large impact on RCF crack growth (Salahi Nezhad et al., 2023). In short, Salahi Nezhad et al. (2023) showed that crack face friction decreases crack growth rates, but also has an impact on the direction by mainly promoting downward growth and hence potentially increases the risk of unpredicted railbreak. Thus, incorporating crack face friction into the 3D model enables the prediction of these effects and could be an important step towards achieving quantitative predictions and potential model validation. As a result, this can improve the efficiency and planning of maintenance procedures on rails, resulting in safer railway operations with lower maintenance costs, which is a major step towards a greener future.

A numerical framework for predicting crack growth and including crack face friction in 2D has been developed in (Salahi Nezhad et al., 2023), where the crack is modeled explicitly. Explicit crack representation requires conforming the crack geometry with the FE mesh, which can be very time-consuming and even restrictive in complex geometries. The crack is thus modeled using XFEM in extending the numerical framework to 3D in (Salahi Nezhad et al., 2024). XFEM offers more flexibility in the crack representation, by enriching the FE approximation in the crack area. This allows the crack modeling to be (almost) independent of the underlying mesh, while the employed enrichment functions capture the discontinuity. In this way, XFEM simplifies meshing for complex geometries and also eliminates the need for remeshing when changing the crack geometry. However, applications of XFEM in commercial software, such as ABAQUS, reported in the literature have largely been limited to frictionless stationary cracks, e.g., see (Andersson et al., 2018, 2020). This motivates investigations of the accuracy and robustness of using XFEM for modeling frictional stationary cracks in 3D in ABAQUS.

## 1.2 Objective

The objective of this master's thesis is to further develop an existing numerical framework in 3D for predicting crack growth direction and rate in rails. More specifically, the aim is to improve the fidelity of the framework developed in (Salahi Nezhad et al., 2024), by incorporating crack face friction and qualitatively evaluating its potential impact on crack growth rate and direction under relevant operational load scenarios. Additionally, since XFEM is employed as a crack modeling approach, the following specific objectives are established:

- Investigation of the accuracy and robustness of XFEM for frictional 3D cracks, and its practical implementation in ABAQUS
- Evaluation of the influence of crack face friction on RCF crack growth rate and direction

## 1.3 Scope and limitations

Frictional crack face contact is implemented in the commercial software ABAQUS. For this, the influence of crack face friction on crack growth rate and direction is investigated without considering its potential interaction with external factors, such as lubrication from water or grease. The study is also limited to incorporating friction in stationary head checks. Additionally, the effects of crack face friction on the crack initiation process are not considered, meaning that the FE model includes an initial crack of a certain size.

The rail material is modeled as a linearly elastic material, and thus cannot capture any potential influence of anisotropy close to the rail surface. Wear-off and residual stresses in the rail are furthermore not taken into account. Finally, microstructural effects are beyond the scope of this study, and modeling parameters are not calibrated against experimental data.

# 2 Modeling frictional crack face contact

This chapter introduces the fundamentals of XFEM versus explicit crack representation in FE analysis, including their respective advantages and limitations. The adopted model for implementing crack face friction constraints is also presented.

## 2.1 Crack representation

In the Finite Element Method (FEM), the displacement field, $\boldsymbol{u}(\boldsymbol{x})$, is approximated over a discretized domain consisting of elements connected by nodes, i.e.,

$$\boldsymbol{u}(\boldsymbol{x}) = \sum_{i=1}^{\mathcal{N}} \boldsymbol{N}_i(\boldsymbol{x})\boldsymbol{a}_i, \tag{1}$$

where $\boldsymbol{N}_i(\boldsymbol{x})$ are the shape functions, $\boldsymbol{a}_i$ are the nodal displacements and $\mathcal{N}$ is the total number of nodes. The accuracy of such an approximation depends on the mesh quality and the type of elements used. However, this discrete formulation poses specific challenges when introducing cracks, since discontinuities must be captured within the discretized geometry. Accurate representation of cracks in numerical models is therefore a major challenge in engineering, and often requires advanced modeling techniques. For this reason, several approaches have been developed in the literature, each with their own advantages and drawbacks.

One way to represent a crack is to do so explicitly, by creating separate node sets in the FE mesh for the upper and lower surface of the crack, as shown in Figure 2.1a. Creating a physical crack in the geometry in this way provides an accurate crack representation, but requires a high quality mesh around the crack, which can be an issue for complex geometries. In addition, the mesh is required to conform to the crack path. For this reason, crack propagation or geometric changes require mesh regeneration, which can be cumbersome (Kuna, 2013).

One way to circumvent these inconveniences, is to incorporate the crack formulation in the FE approximations, as done by XFEM (Belytschko & Black, 1999; Moës et al., 1999). As shown in Figure 2.1b, the idea of XFEM is to enrich the FE approximated displacement field around the crack with additional functions, and thereby inducing displacement discontinuities across the cracked elements (Khoei, 2015).

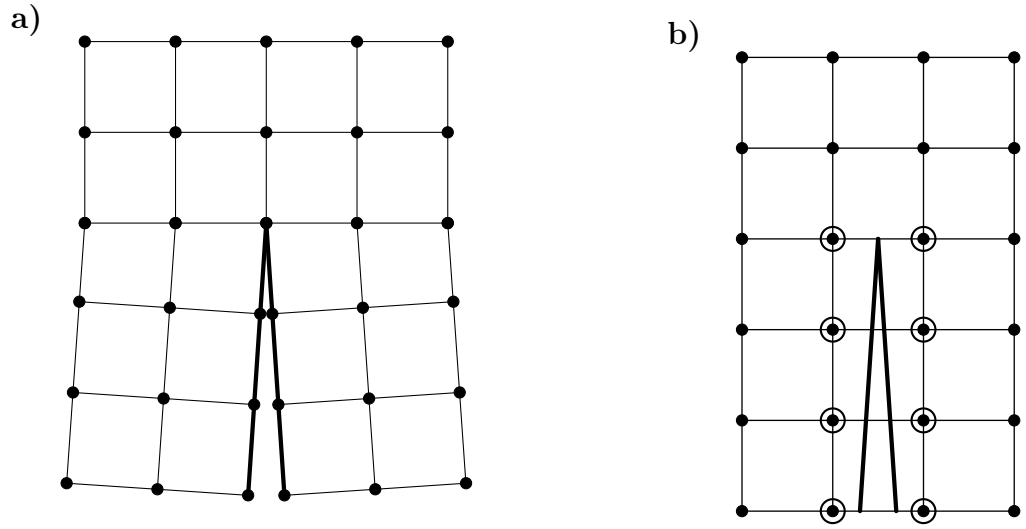


Figure 2.1: Crack Representation in FE mesh using (a) Explicit representation. (b) XFEM, where the enriched nodes are marked with hole circles.

A basic way to define the FE approximated displacement field with an XFEM formulation is as follows (Khoei, 2015):

$$\boldsymbol{u}(\boldsymbol{x}) = \sum_{i=1}^{\mathcal{N}} \boldsymbol{N}_i(\boldsymbol{x})\boldsymbol{a}_i + \sum_{j=1}^{\mathcal{N}^{enr}} \boldsymbol{N}_j(\boldsymbol{x})\boldsymbol{H}(\boldsymbol{x})\boldsymbol{a}_j^{enr}, \tag{2}$$

where $\boldsymbol{a}_j^{enr}$ denote enriched nodal displacements, and $\mathcal{N}^{enr}$ is the number of enriched nodes. Moreover, the Heaviside function $\boldsymbol{H}(\boldsymbol{x})$ can be defined for any point $\boldsymbol{x}$ in the body as

$$\boldsymbol{H}(\boldsymbol{x}) = \begin{cases} 0 \;\text{ if }\; (\boldsymbol{x} - \boldsymbol{x}^*) \cdot \boldsymbol{n} < 0 \\ 1 \;\text{ if }\; (\boldsymbol{x} - \boldsymbol{x}^*) \cdot \boldsymbol{n} > 0, \end{cases} \tag{3}$$

and is referred to as the Heaviside step function. Here, $\boldsymbol{n}$ is the normal vector to the crack at the closest point on the crack plane $\Gamma$, i.e.,

$$\boldsymbol{x}^* = \arg\min_{\hat{\boldsymbol{x}} \in \Gamma} ||\boldsymbol{x} - \hat{\boldsymbol{x}}||.$$

The relation between $\boldsymbol{x}^*$, $\boldsymbol{x}$ and $\boldsymbol{n}$ is illustrated in Figure 2.2.

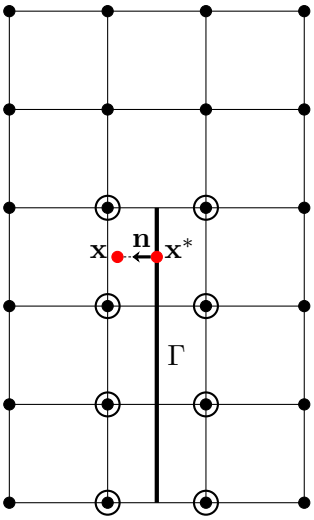


Figure 2.2: Illustration of the geometric relation between the point $\boldsymbol{x}$, the closest point $\boldsymbol{x}^*$ on the crack surface $\Gamma$, and the crack normal vector $\boldsymbol{n}$. Adapted from Salahi Nezhad (2024).

The added enrichment functions allow XFEM cracks to be almost completely independent of the mesh, with the exception of potential numerical issues that can occur if the crack intersects too close to a node. This independence greatly simplifies the meshing process, and also removes the need for time-consuming remeshing efforts with changes in the crack geometry, as long as the crack is still located in a refined mesh area. As a result, and consistent with the motivation presented in (Salahi Nezhad et al., 2024), XFEM is adopted as a crack modeling approach for evaluating the impact of crack face friction on crack growth rate and direction.

## 2.2 Crack face friction constraints

For representation of a realistic crack, especially under compressive and shear loadings, contact constraints at the crack faces are necessary in both normal and tangential directions. The normal contact prevents unrealistic penetration of the crack faces at crack closure under compressive loadings, while the tangential contact controls the presence of crack face friction.

The penalty method, a widely used approach for contact problems in FE analyses (Wriggers, 2006), is employed in this study. In this method, the normal contact pressure, $t_n$, can be expressed as

$$t_n = \epsilon_n g_n \quad \text{for} \quad g_n < 0, \tag{4}$$

where $g_n$ is the gap between the crack faces and $\epsilon_n$ is the penalty parameter. In this study, the penalty parameter was kept as the default value provided by ABAQUS, which is automatically determined from the material stiffness and element size to balance the need to avoid noticeable interpenetration while still maintaining numerical stability.

In the tangential direction, Coulomb's model is utilized for the modeling of crack face friction. The tangential traction between the contacting surfaces, $t_t$, following Coulomb's

model is evaluated as

$$\begin{cases} |t_t| \leq \mu\, t_n & v_t = 0 \text{ (stick)} \\ t_t = -\mu\, t_n \dfrac{v_t}{|v_t|} & v_t \neq 0 \text{ (slip)} \ , \end{cases} \tag{5}$$

where $t_n$ is the normal contact pressure and $v_t$ is the tangential velocity due to slip between the contact surfaces. Further, $\mu$ is the friction coefficent.

# 3 Investigation of XFEM for modeling frictional cracks

This chapter describes the investigation of using XFEM for modeling stationary frictional cracks in 3D simulations in the commercial software ABAQUS.

## 3.1 Preliminaries

As highlighted in Section 1.1, most previous work on XFEM applications for cracks in ABAQUS has involved frictionless stationary cracks. As an example, XFEM was employed for 3D simulations of frictionless cracks in (Salahi Nezhad et al., 2024), while explicit crack representation was used when crack face friction was included in 2D simulations (Salahi Nezhad et al., 2023). This motivates further investigation of applying XFEM to frictional stationary cracks in 3D simulations, since XFEM can significantly simplify the mesh generation process. This is especially relevant for complex geometries such as rail heads, which are of interest in this study.

For validating the use of XFEM for frictional cracks, the contact formulation at the crack faces is the area of interest. One way of confirming that the crack behaves as expected under desired loading is to investigate stresses at the crack faces. For this, an FE model of a simple 3D block is created using the commercial software ANSA and ABAQUS CAE. ANSA is used for building the model, meshing and applying loads and boundary conditions, while the crack geometry is implemented using ABAQUS CAE. In addition, post-processing is performed in MATLAB.

One challenge with modeling XFEM cracks, however, is that there are no physical crack surfaces in the model in terms of separate node sets. Instead, the crack is represented in the FE formulation as displacement discontinuities using enrichment functions. As a result, there is no way of evaluating output parameters directly on the XFEM crack faces in ABAQUS. For this reason, a crack is embedded into a simple block geometry using both XFEM and explicit crack modeling in two separate cases. The explicit model is used to assess the plausability of the friction implementation, and thereby serves as a benchmark for the behavior of the XFEM model. The first part of this chapter presents the simple block model, followed by the crack implementation using explicit crack modeling. The final part covers the XFEM crack implementation and concludes the feasibility study of XFEM as the chosen modeling approach for stationary frictional cracks in 3D simulations.

## 3.2 Simple block model

This section presents the simple 3D block model, along with relevant analytical comparisons for different load sceanarios to ensure reasonable behavior. A rectangular block having a square base with a side length of $W = 100$ mm and a length of $L = 500$ mm is considered. The block is clamped in all directions at the right side, and loaded at the left side with shear, tensile and compressive stresses in three different cases. In each case, the load magnitude is 10 MPa. The loads are applied in the $y$- and $z$-directions, represented by a vertical force $V$ and a longitudinal force $F$, respectively. The resulting homogeneous traction is exemplified in Figure 3.1 for a pure vertical (shear) load $V$ ($F = 0$). Furthermore, the material is assumed to be linearly elastic with a Young's modulus of 210 GPa and a Poisson's ratio of 0.3. The block is discretized using first-order hexahedral elements with an element size of 12.5 mm.

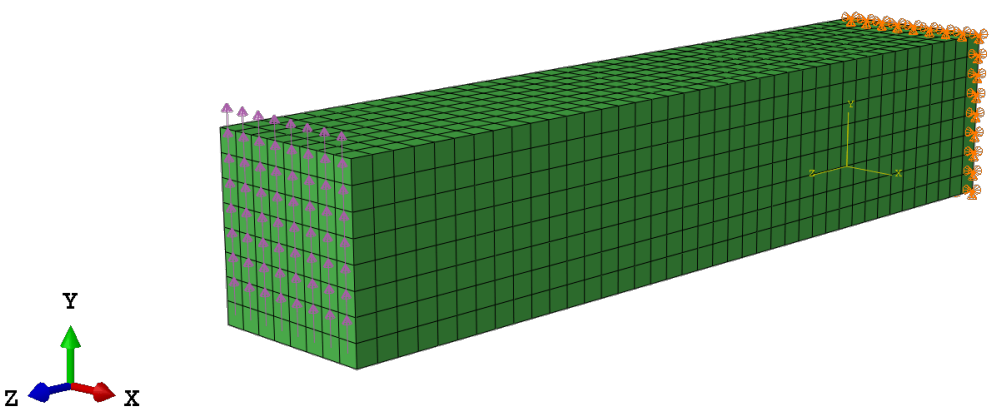


Figure 3.1: Simple block model of $100 \times 100 \times 500$ mm$^3$ subjected to shear loading.

The block can be approximated as a bar element under axial loading (tensile and compressive), and an Euler-Bernoulli cantilever beam with a concentrated traverse load at the free end under shear loading. Analytical formulae in basic solid mechanics given in Equations (6) and (7), expressing displacements on the left side in the load direction for each load case, are then used to compare with numercial results. More specifically, Equation (6) is used for the tensile and compressive load cases, while Equation (7) is employed for shear loading. The displacements from ABAQUS and the analytical values for all load cases are presented in Table 3.1.

$$u_z(L) = \frac{FL}{AE} \tag{6}$$

$$u_y(L) = \frac{VL^3}{3EI} \tag{7}$$

Table 3.1: Displacements on the left side in each load direction

| | $u_z(L)$, tensile load [mm] | $u_z(L)$, compressive load [mm] | $u_y(L)$, shear load [mm] |
|---|---|---|---|
| ABAQUS | 0.0237 | -0.0237 | 2.417 |
| Analytical | 0.0238 | -0.0238 | 2.380 |

Table 3.1 shows that the displacements extracted from ABAQUS are close to the analytical values, considering the element size of the mesh. Additionally, the stress distribution for each load case was found to be consistent with the expected behavior in the analytical models. For instance, negligible shear stresses were found in the tensile and compressive load cases, while the expected parabolic shear stress distribution in the y-direction of the cross section was observed in the shear load case.

## 3.3 Explicit crack on simple block model

This section presents the implementation of a frictional explicit crack in 3D into the block model in Section 3.2, followed by qualitative assessment of the friction modeling. As mentioned in Section 2.2, the penalty method and Coulomb's model are employed to define normal contact and frictional interaction between the crack faces, respectively.

### 3.3.1 Analytical verification of frictionless crack

As a first step, the implementation of a frictionless crack is verified against an analytical expression of the Stress Intensity Factor (SIF) under pure mode I loading $K_I$ (Andersson et al., 2018). A tensile load of 10 MPa is applied on the left side of the block, while it is clamped on the right side. For this, the crack length is defined as $a = W/2 = 50$ mm and placed at height $L/2 = 250$ mm. The mesh is refined in the crack area with an element side length of approximately 1 mm, in alignment with the conditions specified in (Andersson et al., 2018). Figure 3.2 illustrates the block and a scaled displacement response (scale factor of 200) under pure tensile loading, which translates into pure mode I loading at the crack.

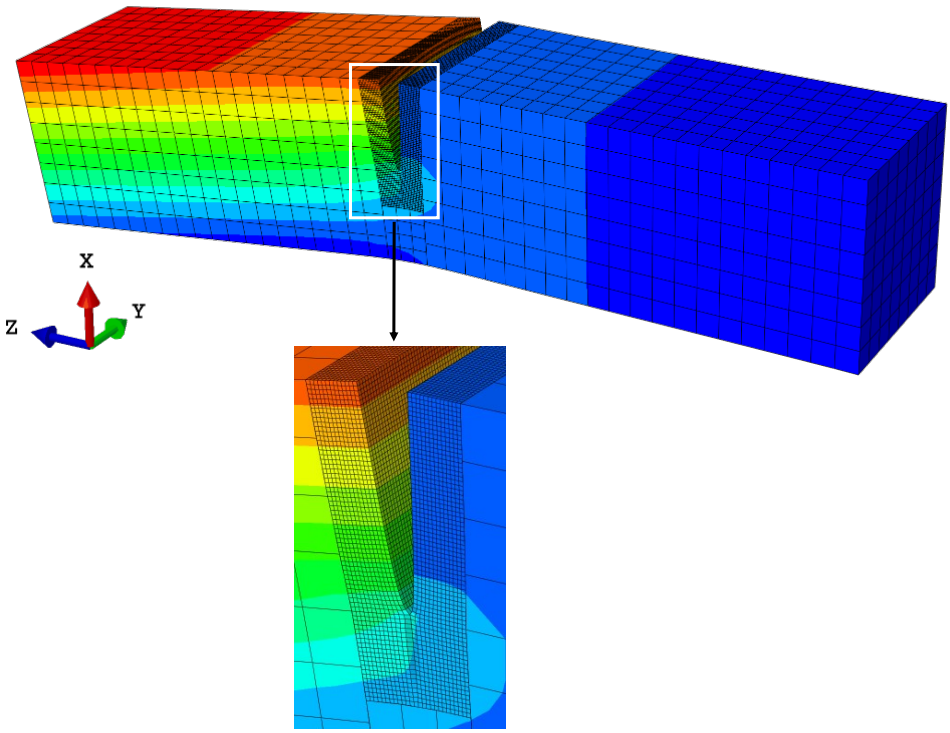


Figure 3.2: Displacement response (scale factor of 200) of explicit crack under pure tensile loading.

The analytical value for $K_I$ is given in (Andersson et al., 2018) as

$$K_I = \sigma\sqrt{\pi a}\left(\frac{\sqrt{\frac{2}{\pi a/W}\tan\left(\frac{\pi a/W}{2}\right)}\left[0.752 + 2.02a/W + 0.37\left(1-\sin\left(\frac{\pi a}{2}\right)\right)^3\right]}{\cos\left(\frac{\pi a/W}{2}\right)}\right) \approx$$

$$\approx 11.2 \text{ MPa} \cdot \sqrt{\text{m}}. \tag{8}$$

In the simulation, $K_I$ is evaluated in the middle of the crack front using the standard ABAQUS implementation of the J-integral (Dassault Systèmes Simulia Corp., 2023b). The obtained numerical value is 11.09 MPa $\cdot \sqrt{\text{m}}$, which shows good agreement with the analytical expression in Equation (8), and thereby verifies the crack implementation.

### 3.3.2 Qualitative assessment of friction implementation

For the assessment of frictional crack face contact, two loading cases are considered: (i) pure shear of 10 MPa and (ii) combined shear–compression, with 10 MPa applied in both shear and compression. In these cases, the shear load is applied in the $y$-direction (see Figure 3.1), and the compression in the $z$-direction. The implementation is evaluated by examining the ABAQUS output variables `CSTATUS` and `CSHEAR2` for friction coefficients $\mu = 0$, $\mu = 0.3$ and $\mu = 0.5$. `CSTATUS` indicates whether two surfaces are in contact and, if so, whether they are sticking or slipping in the tangential direction. `CSHEAR2` provides the corresponding shear stress on the contact surfaces in the direction of the applied shear load. The results for `CSTATUS` for one of the crack faces under pure shear and combined shear–compression loadings are presented in Figure 3.3.

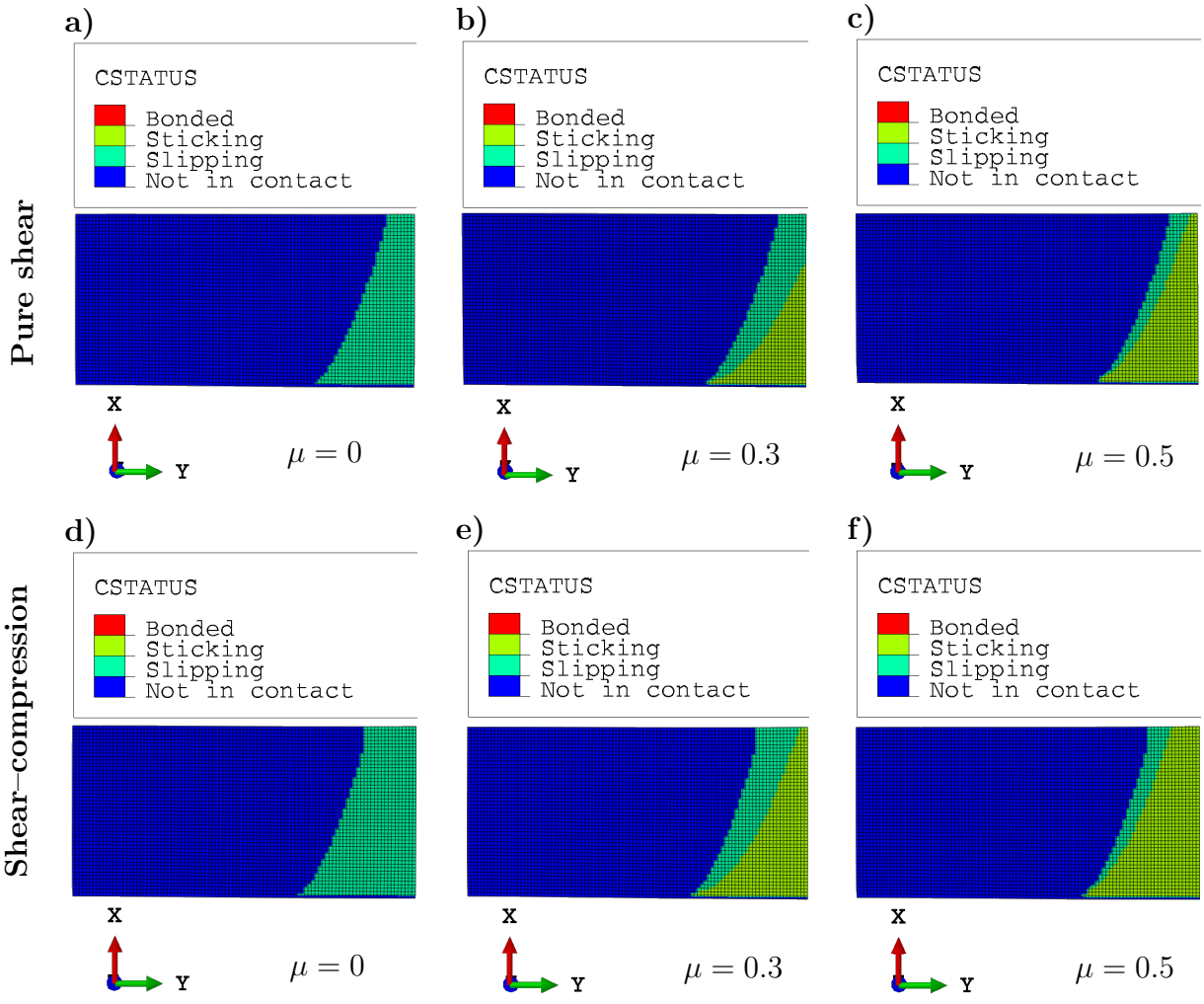


Figure 3.3: CSTATUS results for pure shear (a–c) and combined shear–compression (d–f), for different friction coefficients $\mu$.

In both pure shear and combined shear–compression cases, a frictionless crack yields complete slipping in the contact area between the crack faces. In contrast, introducing friction produces zones of sticking that expand as the friction coefficient increases. This behavior is consistent with theoretical expectations, indicating that the contact formulation and friction model generate reasonable results. It should be noted that the present boundary conditions introduce a slight bending effect in the specimen, which explains the asymmetric contact distribution observed at the crack faces in Figure 3.3.

To further support the conclusion that the contact formulation and friction model generate reasonable results, `CSHEAR2` is evaluated at two locations of the contact area for both load cases, and are denoted 'left contact' (section A–A) and 'right contact' (section B–B) moving forward. Results are evaluated at two locations to increase the amount of data and to ensure that the observed trends are consistent in the area of interest. Figures 3.4 and 3.5 present the curves for `CSHEAR2` for varying friction coefficients and load cases, along with the corresponding evaluation points.

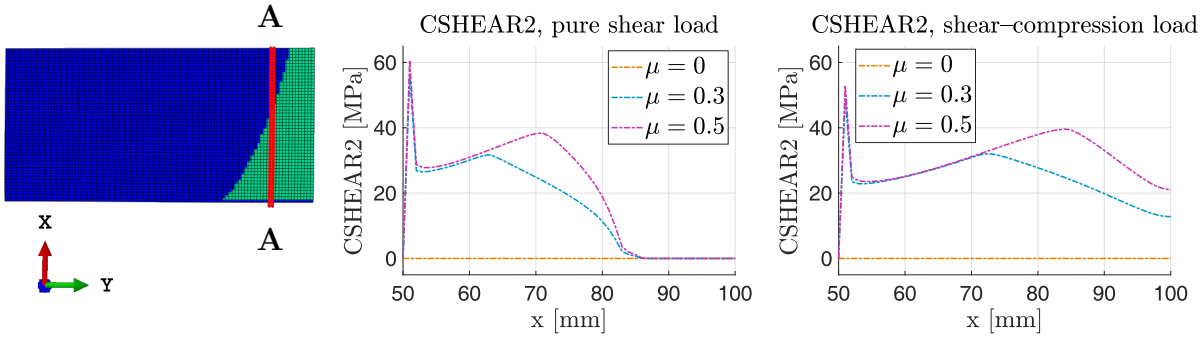


Figure 3.4: Contact shear stress (`CSHEAR2`) results at the left contact side (section A–A) for pure shear and shear–compression loads for different friction coefficients $\mu$.

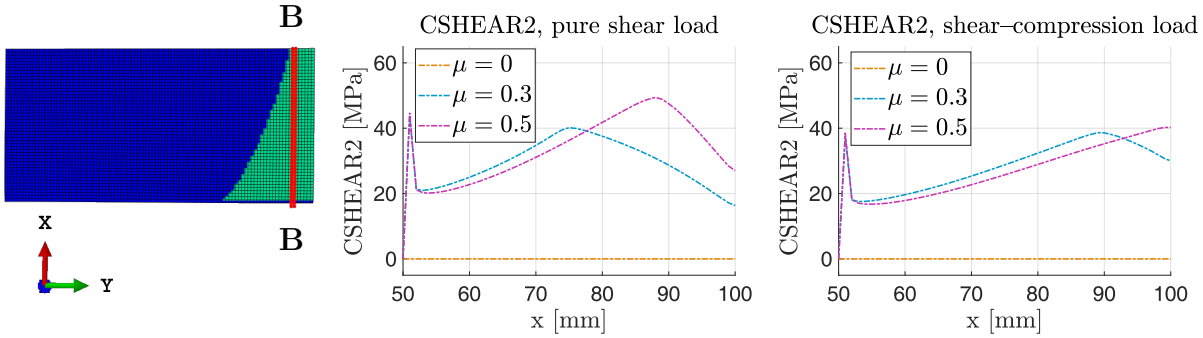


Figure 3.5: Contact shear stress (`CSHEAR2`) results at the right contact side (section B–B) for pure shear and shear–compression loads for different friction coefficients $\mu$.

Figures 3.4 and 3.5 show that `CSHEAR2` is zero for frictionless cracks for both load cases, and increases when friction is included. As expected, the highest stress peaks occur for the friction coefficient $\mu = 0.5$ due to sticking. This behavior is consistent with theory and further supports the plausibility of the friction implementation. Since `CSHEAR2` is not available as a direct ABAQUS output for XFEM cracks, the internal shear stress in the $yz$-direction ($\tau_{yz}$) is instead used as a benchmark for comparison with XFEM.

However, discrepancies were observed when comparing the shear stress evaluated at the contact (CSHEAR2) and the shear stress evaluated in the volume (elements) adjacent to the contact surface ($\tau_{yz}$). This is expected since $\tau_{yz}$ depends on the internal stress distribution as opposed to CSHEAR2, which is the shear stress component on the contact surface. Another factor is that the internal shear stresses are evaluated at integration points inside each element, while the contact shear caused by friction is evaluated directly on the crack surfaces. To reduce the discrepancies, the following three adjusted models were considered: (i) mesh refinement around the crack, (ii) truncated sides to minimize potential bending effects, and (iii) a combination of the two. To illustrate these modifications, the combined truncated and refined model is shown in Figure 3.6. The new length is defined as $L = 73$ mm and the element size in the refined crack area is approximately 0.4 mm.

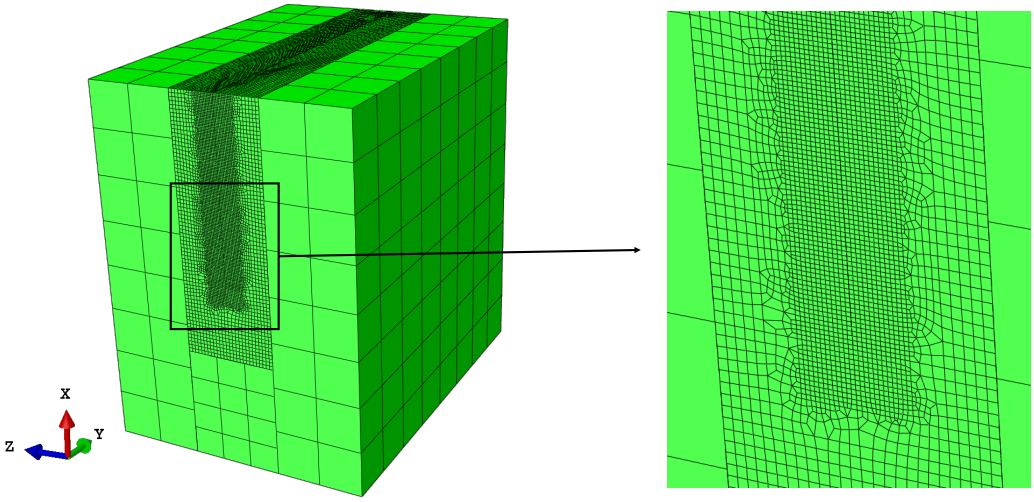


Figure 3.6: Illustration of model variant (iii): truncated sides ($100 \times 100 \times 73$ mm$^3$) and refined mesh around the crack.

In Figures 3.7 and 3.8, the shear stress evaluated at the contact (CSHEAR2) and the shear stress evaluated in the volume (elements) adjacent to the contact surface ($\tau_{yz}$) are presented for the original model and the three adjusted variants. Both represent the shear stress component $\tau_{yz}$ but are obtained in different ways, and are therefore denoted separately here for clarity: $\tau_{yz}$ refers to the bulk stress evaluation at Gauss points, while CSHEAR2 is calculated from the contact formulation. Results are again provided for both load cases and for the left and right sides of the contact area to ensure consistent behavior, with the evaluation points illustrated in Figures 3.4 and 3.5. Moreover, the scaling of the plots is such that differences between $\tau_{yz}$ and CSHEAR2 are highlighted.

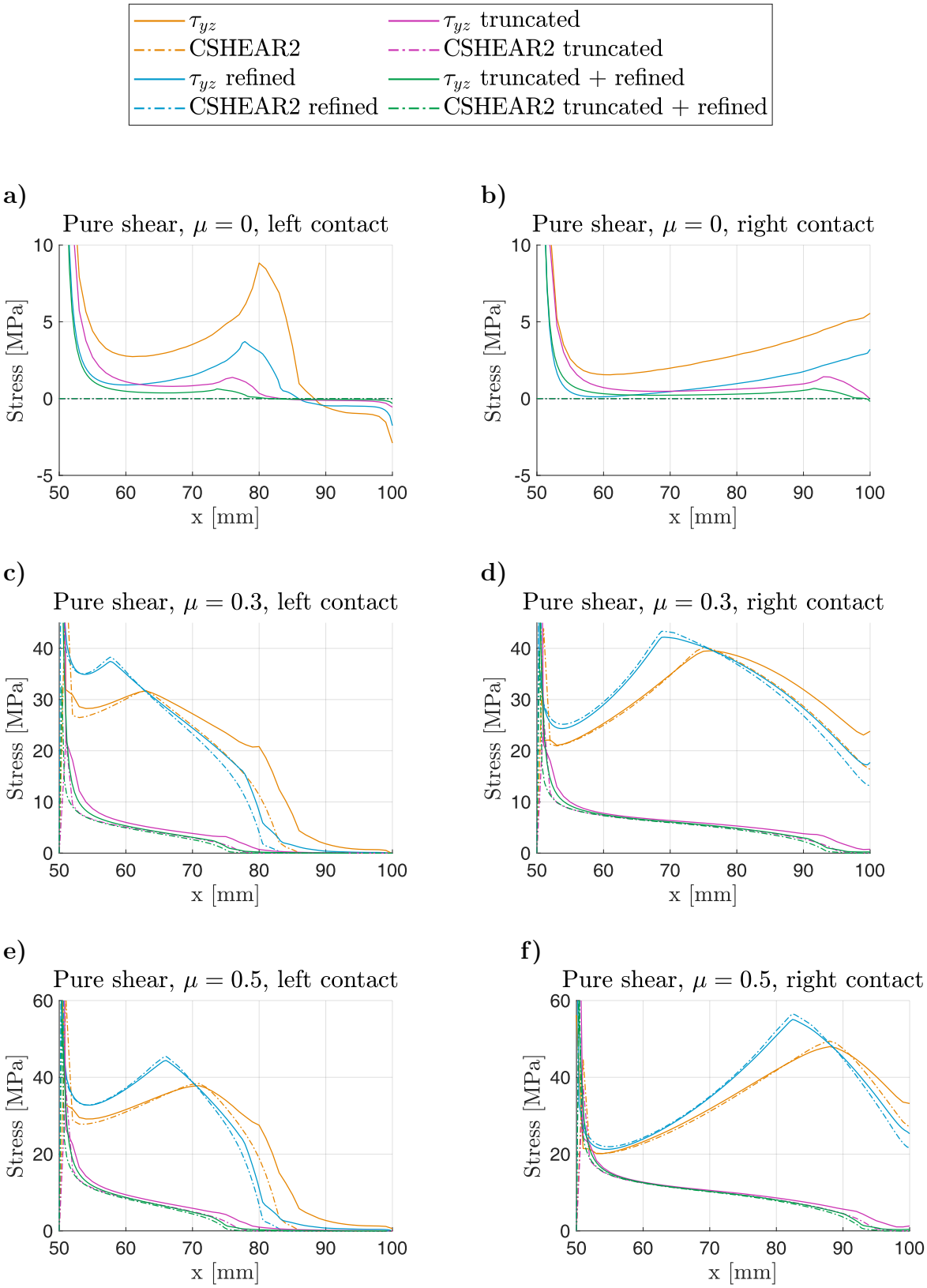


Figure 3.7: Shear stress evaluated at the contact (`CSHEAR2`) and shear stress evaluated in the volume (elements) adjacent to the contact surface ($\tau_{yz}$) under pure shear loading for varying friction coefficients $\mu$. To the left are the left contact side results and to the right are the right contact side results.

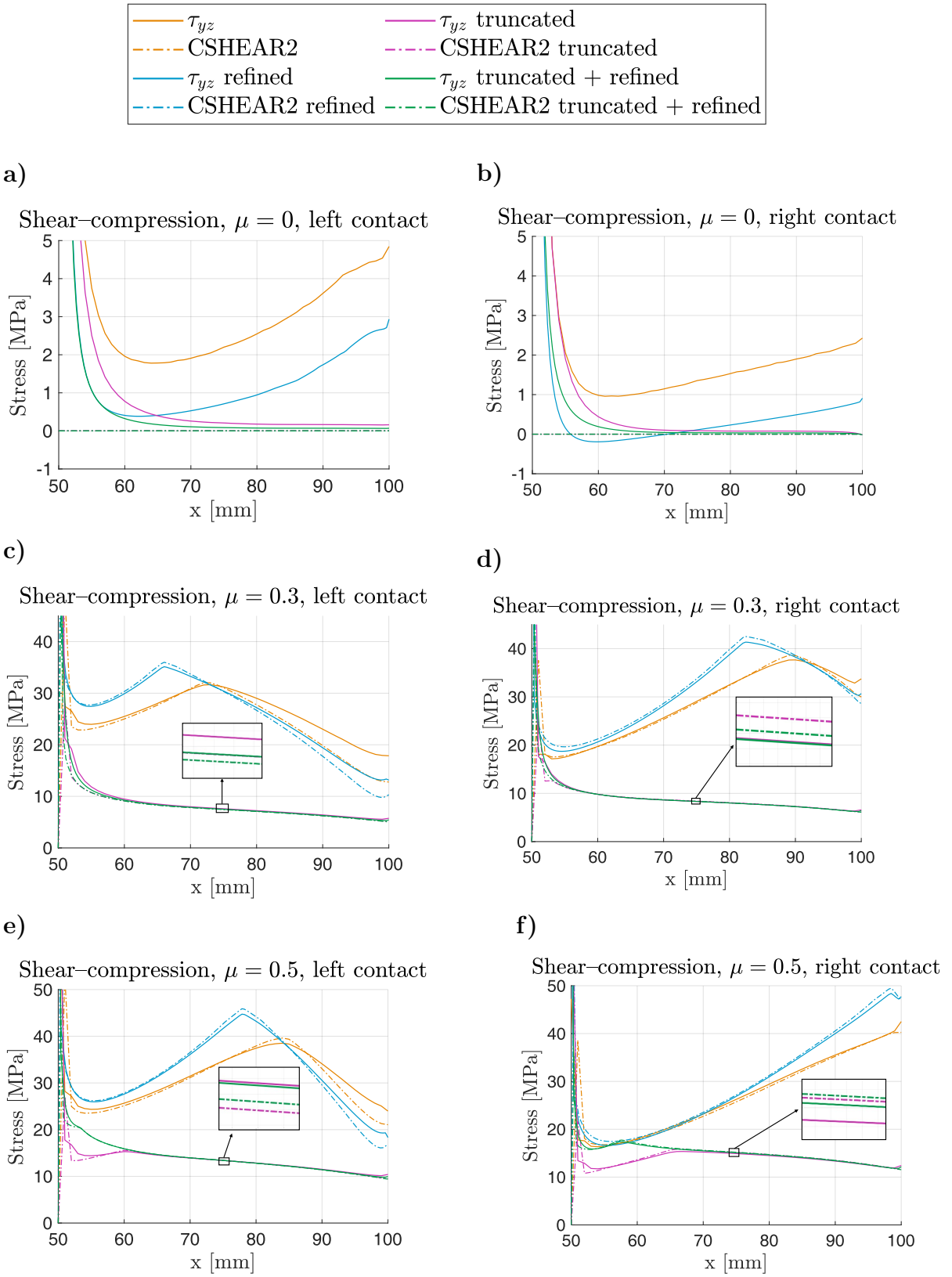


Figure 3.8: Shear stress evaluated at the contact (`CSHEAR2`) and shear stress evaluated in the volume (elements) adjacent to the contact surface ($\tau_{yz}$) under combined shear–compression loading for varying friction coefficients $\mu$. To the left are the left contact side results and to the right are the right contact side results.

Figures 3.7 and 3.8 show that for different block lengths, the curves seem to converge, but towards different reference curves due to the truncation. Moreover, since the accuracy is the lowest near the crack front (around $x = 50$ mm) due to stress singularities, this region is not considered in the evaluation. Discrepancies between $\tau_{yz}$ and `CSHEAR2` are observed for all cases, reflecting numerical differences between the bulk shear stress evaluation and the shear stresses obtained from the contact formulation. In the frictionless cases, these discrepancies provide a direct quantification of the numerical error, since both $\tau_{yz}$ and `CSHEAR2` should theoretically be zero. Further, the results demonstrate that the truncated model exhibits rapid mesh convergence, while the combined truncated and mesh refined model consistently provides the overall smallest discrepancies between $\tau_{yz}$ and `CSHEAR2`, in line with the expected results. Although this model does not ensure complete alignment between $\tau_{yz}$ and `CSHEAR2`, the similar curve trends and lowered discrepancy as model improvements are added, motivate the use of $\tau_{yz}$ as a suitable reference for the case of XFEM cracks.

## 3.4 XFEM crack on truncated simple block model

This section describes the implementation of a frictional crack using XFEM on the truncated and refined block model described in Section 3.3.2. Additionally, results from comparing shear stresses of the explicit and XFEM cracks are presented.

### 3.4.1 Implementation of stationary frictional cracks in ABAQUS

Due to difficulties in implementing frictional contact with the same formulation as for the explicit crack, alternative approaches were explored. Further investigations indicated that the challenges of the contact implementation in ABAQUS are linked to the stationarity of the XFEM crack. Upon finding that allowing for propagation resulted in more realistic shear stresses as friction was included, an approach of inducing stationarity while allowing for propagation, was adopted.

This approach includes establishing a damage criterion for the material by defining thresholds for damage initiation and damage evolution. In this study, the *Quads* criterion is adopted for damage initiation, where nominal stresses in each direction are defined, and a combination of these serves as a threshold for initiating fracture (Dassault Systèmes Simulia Corp., 2023d, Defining damage). Possible damage evolution is defined through critical energy release rates with a mixed-mode criterion (Dassault Systèmes Simulia Corp., 2023c, Damage evolution). This method allows full control over both the damage initiation and evolution by adjusting the critical nominal stresses and energy release rates. Thus, propagation is prevented by significantly increasing the critical nominal stresses and energy release rates for the material. To ensure stationarity, the ABAQUS output variables `STATUSXFEM` and `SDEG` are examined after simulations. `STATUSXFEM` identifies cracked elements by assigning a value of 1 to cracked elements and 0 to uncracked ones, which allows verification that no additional elements have cracked after loading. `SDEG` instead quantifies material degradation on a scale from 0 to 1. Hence, by confirming that no intermediate values ($0 <$ `SDEG` $< 1$) occur, it can be ensured that no damage evolution has been initiated.

### 3.4.2 Computed shear stresses for XFEM versus explicit crack

Figure 3.9 shows shear stresses $\tau_{yz}$ for a frictional XFEM crack, using the method of forcing stationarity while allowing for propagation, compared to the explicit crack results for the truncated and refined model presented in Section 3.3.2. The results are presented for both load cases at the left and right side of the contact area. Furthermore, the plots are scaled to exclude the parts representing stress singularities at the crack front.

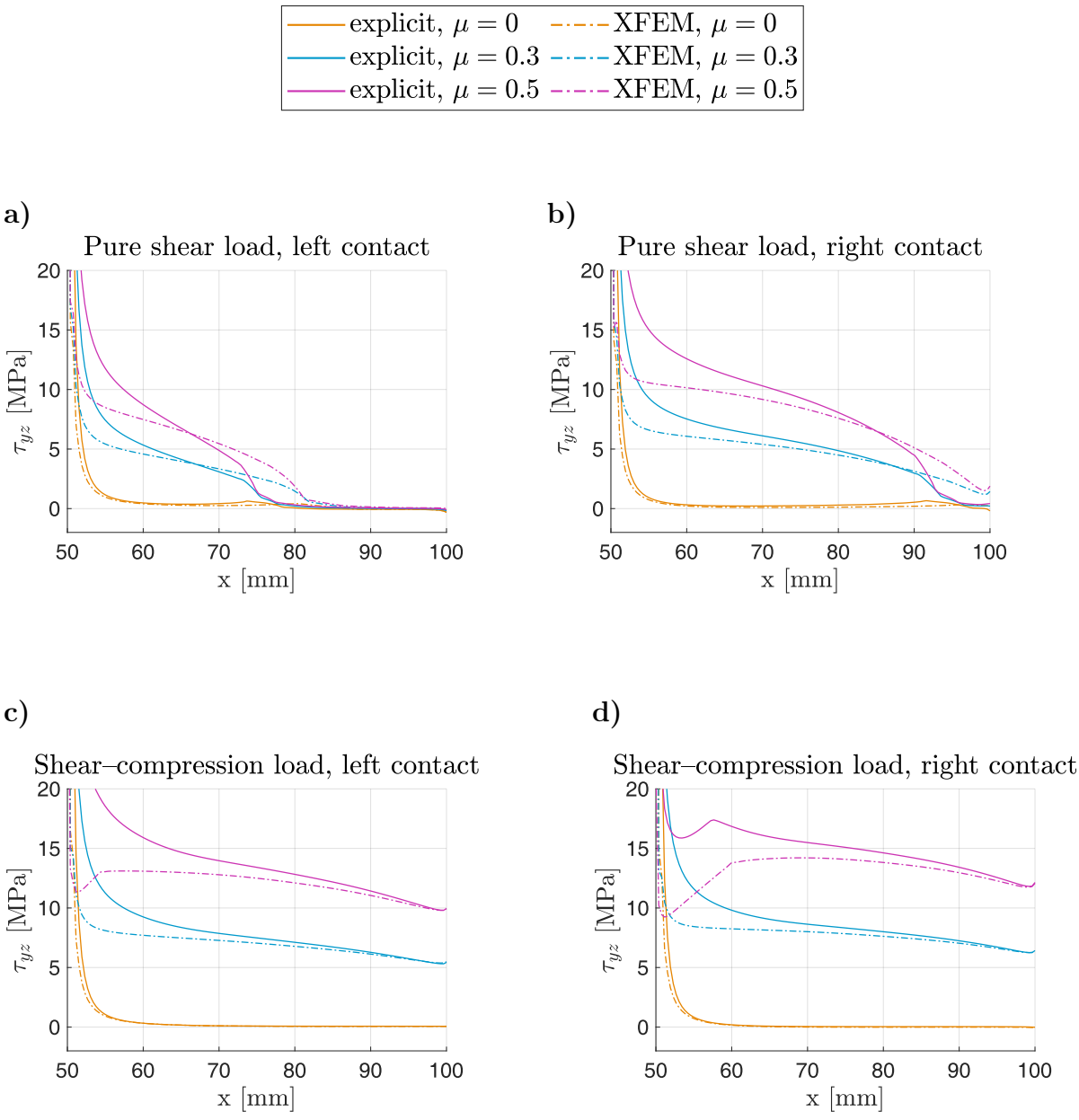


Figure 3.9: Comparison of $\tau_{yz}$ between XFEM and explicit crack representation at different contact sides (see Figures 3.4 and 3.5) and under varying loadings. (a) Pure shear loading at the left contact side. (b) Pure shear loading at the right contact side. (c) Combined shear-compression loading at the left contact side. (d) Combined shear-compression loading at the right contact side.

Figure 3.9 shows that the trends of the curves are similar when comparing explicit crack modeling and XFEM, and that the shear stresses increase as the friction coefficient increases. However, some discrepancies are observed, especially for the frictional cases. Several factors may contribute to these discrepancies. First, stationarity is enforced by allowing crack propagation but suppressing it through parameter adjustments. Although stationarity checks are performed, differences may still arise in how propagating and stationary cracks are treated in ABAQUS. In addition, enriched elements contain non-polynomial and discontinuous enrichment functions, for which standard FE Gauss quadrature is not exact and the number of integration points needs to be increased (Khoei, 2015). Depending on how this is handled internally in ABAQUS, it may reduce accuracy. Moreover, since Figure 3.9 shows internal shear stresses, they are particularly sensitive to mesh size, boundary conditions and other modeling choices, which may further amplify minor differences. Overall, given that the general trends in Figure 3.9 are very similar, and since the present study aims for qualitative comparisons, it can be concluded that XFEM is a suitable approach for representing frictional stationary cracks in 3D simulations in ABAQUS within the scope of this work.

# 4 Simulation of crack growth in rails

This chapter presents the procedure and results for evaluating the influence of crack face friction on crack growth rate and direction in a 3D rail model. The first section describes the FE model used for simulating crack growth in rails using ABAQUS, along with relevant loading scenarios. Methods for evaluating crack growth rate and direction are also presented. The final section presents the simulation results for different operational load scenarios.

## 4.1 FE model and loading scenarios

When a wheel passes along a rail section, a large wheel–rail load is transmitted to the rail through a small contact patch at the rail head, producing high local stresses. Additionally, the wheel–rail load induces bending of the rail. There are also other loads present in rails. As an example, in continuosly welded rails, thermal stresses can arise due to restrictions when the temperature changes. For the scope of this study however, loading scenarios are limited to wheel–rail contact load and rail bending.

### 4.1.1 FE model

Following Salahi Nezhad et al. (2024), the FE model features a rail section of a 60E1 rail profile with a length of 300 mm and a height of 172 mm. Linear elasticity is assumed for the rail material with $E = 210$ GPa and $\nu = 0.3$, and standard first-order hexahedral elements are used for mesh generation.

A semi-circular crack is implemented for different radii at the gauge corner of the rail section located at $(x, y, z)$=(-26.0, -2.3, 150) mm, with an inclination of 25° w.r.t. the longitudinal direction of the rail ($z$-axis) and 27° w.r.t. the lateral direction of the rail ($x$-axis). The mesh around the crack is refined to an element side length of 0.4 mm. Figure 4.1 illustrates the rail section and the crack.

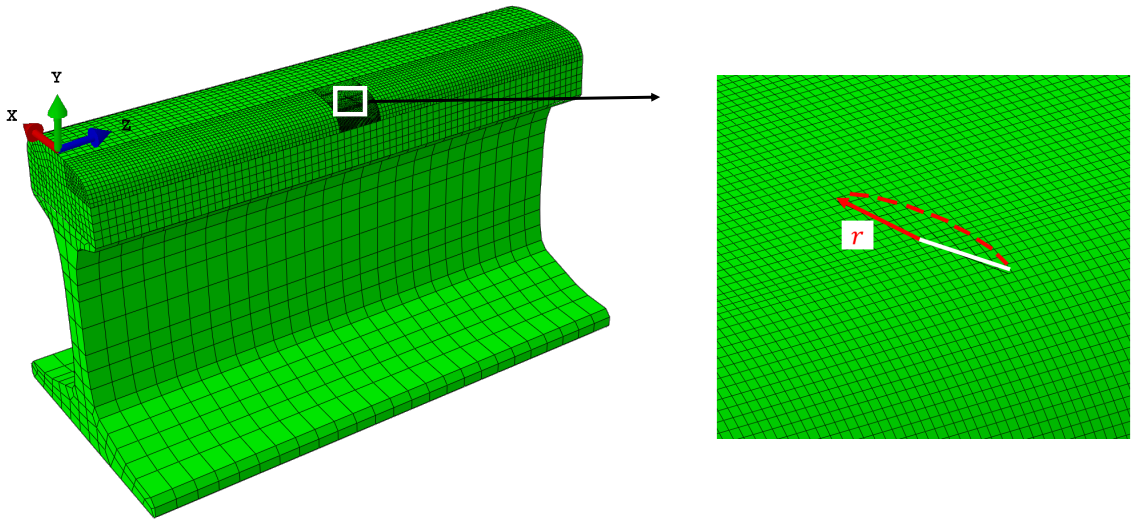


Figure 4.1: Illustration of rail section with a a semi-circular crack with radius $r$.

The crack is assumed to be stationary following the approach presented in Section 3.4, i.e., having a propagating crack in ABAQUS while ensuring its stationarity through parameter adjustments. Contact at crack closure and frictional crack faces are furthermore considered using the penalty method and Coulomb's model, as described in Section 2.2.

### 4.1.2 Contact load

Following Salahi Nezhad et al. (2024), the wheel–rail contact load is considered as a combination of contact pressure and tractive forces in the longitudinal ($z$-)direction. In this study, lateral tractive forces are disregarded. The contact pressure is modeled using Hertzian theory, yielding an elliptic contact area and pressure distribution between the wheel and rail. The contact pressure distribution in the contact patch is defined as

$$p(\bar{x},\bar{z};x,z)=\begin{cases}\frac{3P}{2\pi ab}\sqrt{1-\left(\frac{x-\bar{x}}{a}\right)^2-\left(\frac{z-\bar{z}}{b}\right)^2} & \text{for} \quad \left(\frac{x-\bar{x}}{a}\right)^2+\left(\frac{z-\bar{z}}{b}\right)^2\leq 1\\ 0 & \text{for} \quad \left(\frac{x-\bar{x}}{a}\right)^2+\left(\frac{z-\bar{z}}{b}\right)^2>1.\end{cases} \tag{9}$$

Here, $P$ is the magnitude of the contact load, which is set to 7.5 t in this study. Moreover, $a$ and $b$ are semi-axes of the patch and ($\bar{x}$, $\bar{z}$) is the wheel load position. The tractive forces in the $z$-direction $T_z$, are evaluted by assuming full slip conditions with a traction coefficient $f_{wr}$, such that $T_z = f_{wr}P$. In this study, $f_{wr} = 0.3$ is used. More details regarding implementation of this loading scenario and parameter calculations are presented in (Salahi Nezhad et al., 2024).

To simulate the passing wheels on the rail section, the centre of the contact load is incremented in the $z$-direction over 100 steps. The incrementation is such that most steps are located around the crack since this is the most critical area for considering crack deformation. Furthermore, for the case of pure wheel–rail contact load, the side surfaces of the rail section are clamped in the longitudinal ($z$-)direction. The bottom is clamped in the $x$- and $y$-directions.

### 4.1.3 Rail bending load

Following Salahi Nezhad et al. (2024), longitudinal bending of the rail is obtained from a vertical dynamic vehicle-track interaction analysis in DIFF (Nielsen & Igeland, 1995). In this analysis, a wheel load of 7.5 t passes a smooth track section at 100 km/h. More details regarding the employed ballasted track parameters are presented in (Salahi Nezhad et al., 2022). The bending moment at the location of the crack is thus computed as a function of the wheel load position $\bar{z}$, and can be illustrated in Figure 4.2. The reference position of the wheel load in Figure 4.2 is at the centre of the crack where $\bar{z} = 0.15$ m. The crack is subjected to longitudinal tensile stresses before and after the wheel passes, and compressive longitudinal stresses when the contact is exactly on top of the crack-mouth. The rail bending is applied to the rail FE model in ABAQUS as prescribed boundary displacements on the side surfaces, following Euler-Bernoulli beam theory such that

$$u_z^p(\bar{z};x,y,\frac{L}{2}\pm\frac{L}{2})=\frac{\pm M(\bar{z})\left[h_c+y\right]L}{2EI_x}. \tag{10}$$

Here, $M(\bar{z})$ is the bending moment, $h_c = 0.091$ m is the vertical distance from the top surface of the rail to the neutral axis, and $I_x = 30\cdot 10^{-6}$ m$^4$ is the moment of inertia. For the simulation of rail bending load, the bottom is clamped in the $x$- and $y$-direction.

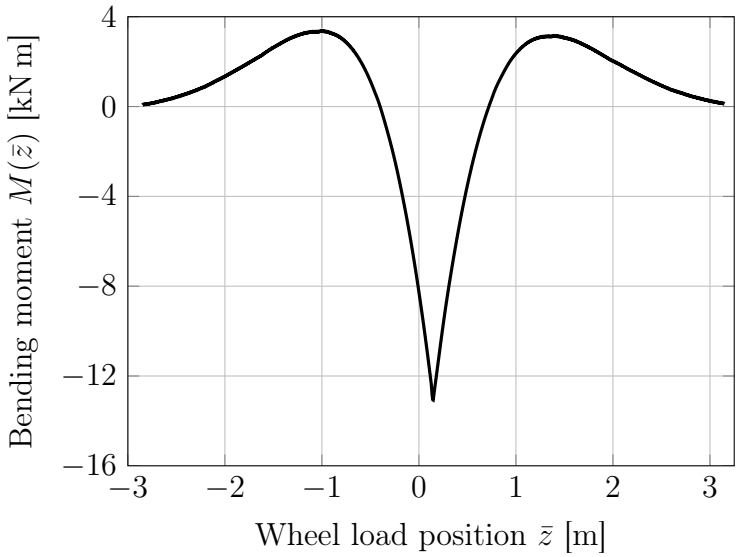


Figure 4.2: Bending moment as function of the wheel load position at the location of the crack. Adapted from Salahi Nezhad et al. (2024).

## 4.2 Evaluation of crack growth rate and direction

This section presents the methods for evaluating crack growth rates and initial crack growth directions in the rail section after a load cycle. Following Salahi Nezhad et al. (2024), the directions are predicted using a modified Vector Crack Tip Displacement (VCTD) criterion, while the rates are evaluated using Paris-type laws that account for various mode interactions.

Both of these methods require SIFs ($K_{\mathrm{I}}$, $K_{\mathrm{II}}$, and $K_{\mathrm{III}}$) along the crack front, which therefore constitute the governing parameters for crack growth rates and direction. In this study, they are evaluated using a built-in ABAQUS implementation feature for three different points along the crack front. Following Salahi Nezhad et al. (2024), the locations of the points relative to the crack front and contact patch are illustrated in Figure 4.3.

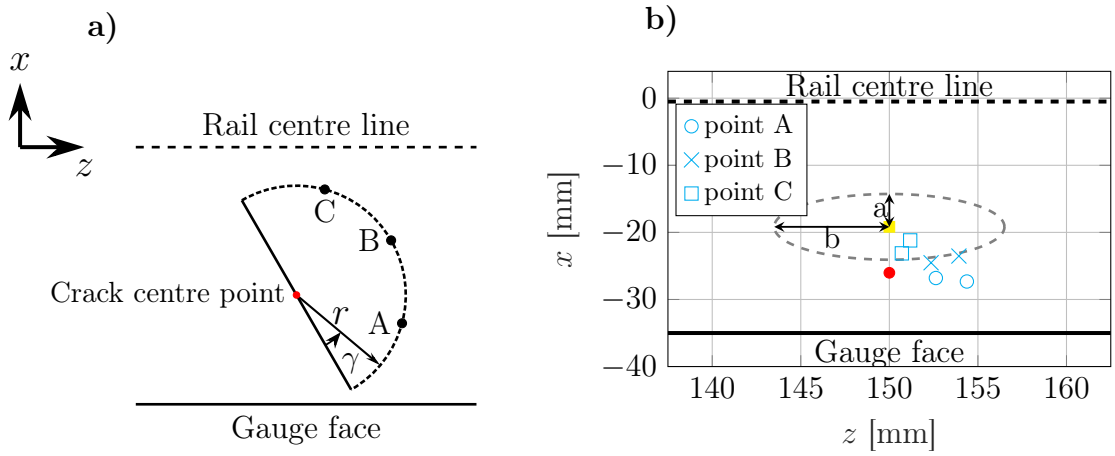


Figure 4.3: Locations of evaluation points A, B and C relative to (a) The crack plane. (b) The contact patch from the wheel–rail load. Adapted from Salahi Nezhad et al. (2024).

### 4.2.1 Crack growth rate

As proposed in (Salahi Nezhad et al., 2024), this study employs two Paris-type laws to account for different mode interactions. For this, a lower estimate of the total growth rate is calculated by assuming sequential loading without any overlap, and thus zero mode interaction, i.e.,

$$\left(\frac{da}{dN}\right)_{\text{lower}} = C\left(\Delta K_{\text{I}}\right)^m + C\left(\Delta K_{\text{II}}\right)^m + C\left(\frac{\Delta K_{\text{III}}}{\sqrt{1-\nu}}\right)^m. \tag{11}$$

Here, $\Delta K = \max_t(K(t)) - \min_t(K(t))$ is the range of the SIF. Note that the negative $K_{\text{I}}$ values are truncated to remove the influence of crack face penetrations in the simulations. The upper estimate instead represents full mode interaction by assuming that the loads are applied simultaneously, and is expressed as

$$\left(\frac{da}{dN}\right)_{\text{upper}} = C\left(\Delta K_{\text{eq}}\right)^m, \tag{12}$$

where $\Delta K_{\text{eq}}$ is computed as

$$\Delta K_{\text{eq}} = \sqrt{\Delta K_{\text{I}}^2 + \Delta K_{\text{II}}^2 + \frac{1}{1-\nu}\Delta K_{\text{III}}^2}.$$

In this study, the material parameters $C = 2.47 \cdot 10^{-9}\ \frac{\text{mm/cycle}}{(MPa\sqrt{m})^m}$ and $m = 3.33$ are employed following Salahi Nezhad et al. (2024).

### 4.2.2 Crack growth direction

To predict the initial crack growth direction after a load cycle, an accumulated VCTD criterion that accounts for non-proportional loading is adopted, following Salahi Nezhad et al. (2024). In this criterion, crack face opening displacements, $\delta_{\text{I}}(t)$, and crack face sliding displacements, $\delta_{\text{II}}(t)$, are evaluated at each time instance $t$ of the load cycle. Thus, any influence of mode III on the crack growth direction is neglected due to limitations of

the criterion. The crack face displacements are computed at a distance $d$ from the crack tip, as the difference between top and bottom surface crack face displacements ($\vartheta = \pi$ and $\vartheta = -\pi$) under plain strain conditions in a local coordinate system of the crack, see Figure 4.4. The radial distance from the crack front is in this study set to $d = 1$ mm. The crack face displacements are calculated as

$$\delta_{\mathrm{I}}(d,t) = u_{\perp}(d,\pi,t) - u_{\perp}(d,-\pi,t) = \boldsymbol{B}(d)K_{\mathrm{I}}(t), \tag{13}$$

$$\delta_{\mathrm{II}}(d,t) = u_{||}(d,\pi,t) - u_{||}(d,-\pi,t) = \boldsymbol{B}(d)K_{\mathrm{II}}(t), \tag{14}$$

where $\boldsymbol{B}(d)$ is defined as

$$\boldsymbol{B}(d) = \frac{8(1-\nu^2)}{E}\sqrt{\frac{d}{2\pi}}.$$

The crack driving displacement vector, $\Delta\boldsymbol{c}$, is defined as

$$\Delta\boldsymbol{c} = \int_0^{T_c} \langle \frac{d\delta_a(t)}{dt} \rangle \, \hat{\boldsymbol{e}}_{\vartheta}(t)\, dt, \tag{15}$$

where $T_c$ is the load cycle duration and $\hat{\boldsymbol{e}}_{\vartheta}(t)$ is the unit vector in the direction of the instantaneous crack growth direction, which in turn is computed as $\vartheta(t) = \arcsin\left(\frac{-\tilde{\delta}_{\mathrm{II}}(t)}{\delta_a(t)}\right)$. Further, $\langle \bullet \rangle = \frac{1}{2}(\bullet + |\bullet|)$ denote Macaulay brackets and the instantaneous crack growth direction $\delta_a(t)$ is expressed as

$$\delta_a(t) = \sqrt{\langle \tilde{\delta}_{\mathrm{I}}(t) \rangle^2 + 2\langle \tilde{\delta}_{\mathrm{I}}(t) \rangle \, |\tilde{\delta}_{\mathrm{II}}(t)| + 2\big(\tilde{\delta}_{\mathrm{II}}(t)\big)^2}. \tag{16}$$

Here, the amplitudes $\tilde{\delta}_{\mathrm{I/II}}(t)$ of $\delta_{\mathrm{I}}(t)$ and $\delta_{\mathrm{II}}(t)$ are defined using

$$\tilde{\delta}_{\mathrm{I/II}}(t) = \delta_{\mathrm{I/II}}(t) - \overline{\delta}_{\mathrm{I/II}}, \qquad \overline{\delta}_{\mathrm{I/II}} = \tfrac{1}{2}\left[\max_t(\delta_{\mathrm{I/II}}(t)) + \min_t(\delta_{\mathrm{I/II}}(t))\right]. \tag{17}$$

Lastly, the accumulated crack growth direction for a load cycle is calculated as a unit vector in the direction of $\Delta\boldsymbol{c}$ as

$$\hat{\boldsymbol{e}}_{\phi} = \frac{\Delta\boldsymbol{c}}{||\Delta\boldsymbol{c}||}. \tag{18}$$

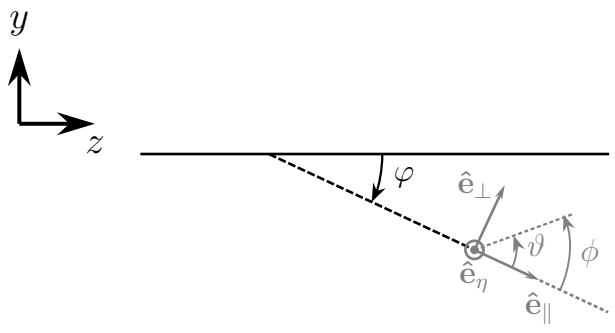


Figure 4.4: Local coordinate system of the crack. The inclined black dashed line indicates the initial inclination of the crack plane w.r.t. the z-axis. Adapted from Salahi Nezhad et al. (2024).

## 4.3 Simulation results for frictional crack in rails

In this section, simulation results for evaluating crack growth rates and directions are presented. The FE model is implemented in ABAQUS following Section 4.1.1, with two different load cases: pure contact load and a combined contact and bending load (see Sections 4.1.2 and 4.1.3). Post-processing to evaluate crack growth rates and directions according to Section 4.2 is performed in MATLAB (The MathWorks, Inc., 2022). To assess the influence of crack face friction, three friction coefficients are examined for both load cases: $\mu = 0$, $\mu = 0.3$, and $\mu = 0.5$. In addition, two different crack radii, $r = 3$ mm and $r = 5$ mm, are considered in order to assess potential effects of crack size, given that this study is restricted to stationary cracks. Stationarity of the frictional cracks is induced following Section 3.4.1.

For the predicted growth direction $\phi$, a local coordinate system of the crack is considered (see Figure 4.4). As a reference point, $\phi = 0$ is the initial slope of the crack, and $\phi < 0$ means that the crack grows downward while $\phi > 0$ represents upward growth.

### 4.3.1 Pure contact loading

For the pure contact load case, a wheel load of 7.5 t with a traction coefficient of $f_{wr} = 0.3$ is applied, as described in Section 4.1.2. Figure 4.5 shows the predicted crack growth rates for point A, B and C and for the different friction coefficients and radii. For this, the upper and lower estimates of the crack growth rates are included in Figure 4.5a, where both the upper and lower estimates show the same trends. Since this behavior was observed for all points, only the upper (most critical) estimates are shown in Figures 4.5b and 4.5c. The predicted crack growth directions for all points, radii and friction coefficients are presented in Figure 4.6.

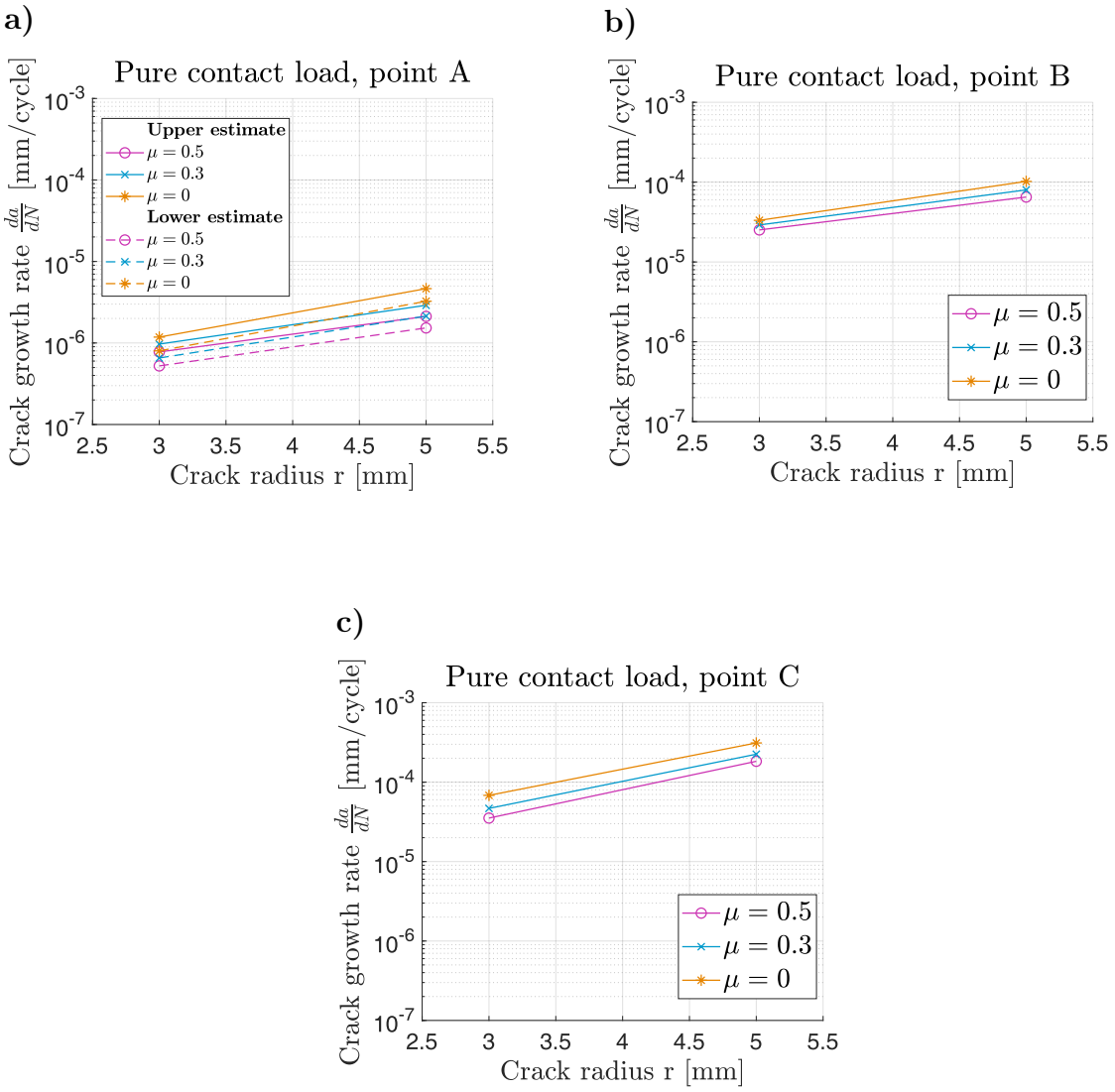


Figure 4.5: Predicted crack growth rates under pure contact load at different evaluation points for varying radii and friction coefficients. (a) Point A (upper and lower estimates). (b) Point B (upper estimate). (c) Point C (upper estimate).

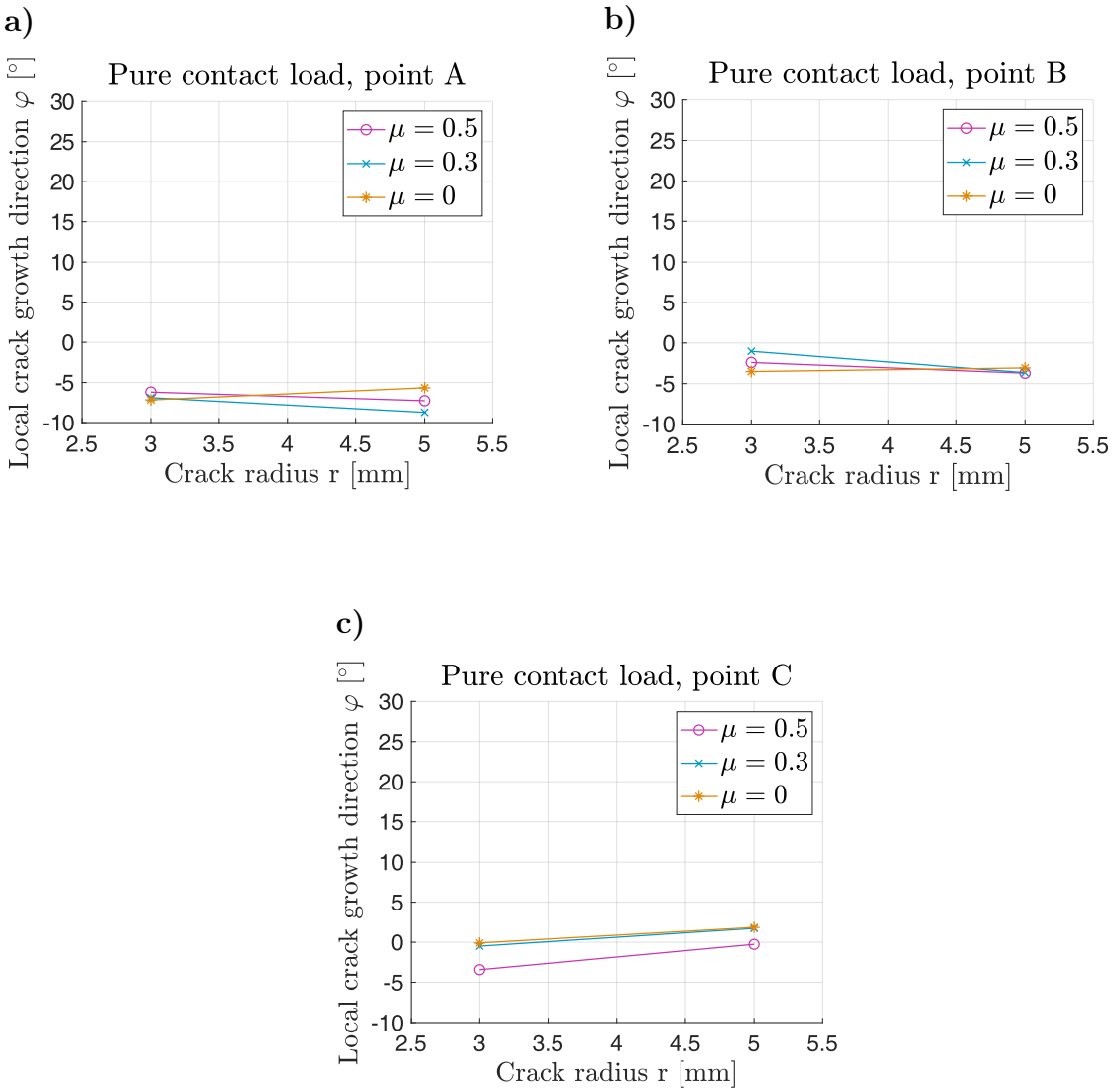


Figure 4.6: Predicted crack growth directions under pure contact load at different evaluation points for varying radii and friction coefficients. (a) Point A. (b) Point B. (c) Point C.

For the predicted crack growth rates, point C exhibits the highest values, followed by points B and A. This can be explained by point C being located closest to the contact load, which increases its influence on the crack loading (i.e., SIFs) and thereby the growth rates. Moreover, increasing the crack radius from 3 to 5 mm leads to higher growth rates for all points. For points B and C, this effect is again attributed to their closer distance to the contact load (see Figure 4.3b), while for point A it is more likely a consequence of boundary effects (Salahi Nezhad et al., 2024).

For all points and both radii, introducing crack face friction and increasing the friction coefficient reduces the crack growth rate. Since the rates are presented on a logarithmic scale in Figure 4.5, differences may appear visually subtle although they correspond to substantial relative changes. For pure contact load, a friction coefficient of 0.5 results in up to a 54% reduction in growth rate compared to the frictionless crack, while a coefficient of 0.3 gives a reduction of up to 37%. The reduction occurs since friction promotes sticking between the crack faces, which limits the relative sliding and shearing displacements

of the crack faces. As a result, the mode II and III loadings are reduced without affecting mode I loading, leading to lower predicted crack growth rates.

Furthermore, increasing the crack radius slightly amplifies the difference between frictionless and frictional cracks for point A and B. The exception for point C may be attributed to its proximity to the peak contact load, which in turn could promote crack closure. For a radius of 3 mm, the largest relative reduction in growth rate between the frictionless case and a friction coefficient of 0.5 is 48%, while for a radius of 5 mm the corresponding reduction reaches 54%. This can be explained by the larger crack faces providing a greater area of sticking, which suppresses more of the sliding and shearing displacements. As a result, the mode II and III SIFs, and thereby the growth rates, are reduced. However, it should be noted that only two radii are investigated, which is insufficient to establish a general trend of larger radii leading to an increased influence of friction.

For the predicted crack growth directions, Figure 4.6 predominantly shows downward growth. This trend was also observed in (Salahi Nezhad et al., 2024) for a frictionless crack under pure contact load. Moreover, the differences between the friction coefficients are too small to be regarded as significant, since the adopted VCTD criterion does not provide that level of accuracy. Salahi Nezhad et al. (2023) investigated the influence of crack face friction in a 2D model of the rail and concluded that, within that framework, frictional cracks tend to promote more downward growth. Although point C shows minor indications of this effect, the differences observed for these radii are not large enough to establish the general influence of crack face friction on the growth directions. In addition, since the study is limited to two radii, it is difficult to determine whether there is a trend in the results for the influence of friction on the growth direction.

### 4.3.2 Combined bending and contact loading

For the case of combined contact and bending load, a combination of bending and a wheel load of 7.5 t with $f_{wr} = 0.3$ is studied, following load parameters and procedures described in Sections 4.1.2 and 4.1.3. Figure 4.7 shows the predicted crack growth rates for point A, B and C and for the different friction coefficients and radii. As for the pure contact load case, the growth rates for the upper and lower estimates show the same trends as in Figure 4.7a. Hence, only the upper (most critical) estimates are shown in Figures 4.7b and 4.7c. The predicted crack growth directions for all points, radii and friction coefficients are presented in Figure 4.8.

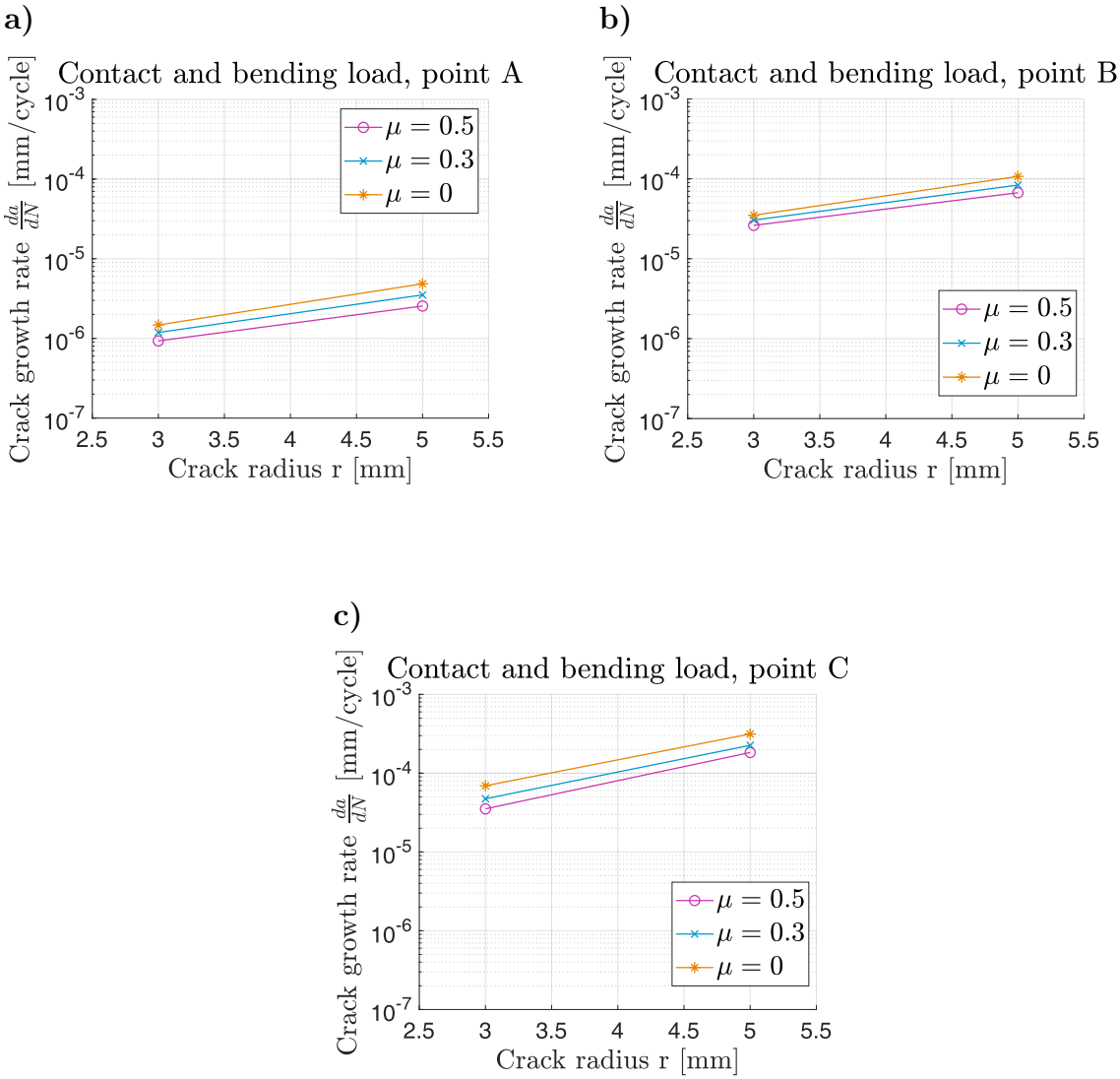


Figure 4.7: Predicted crack growth rates under combined contact and bending load at different evaluation points for varying radii and friction coefficients. (a) Point A. (b) Point B. (c) Point C.

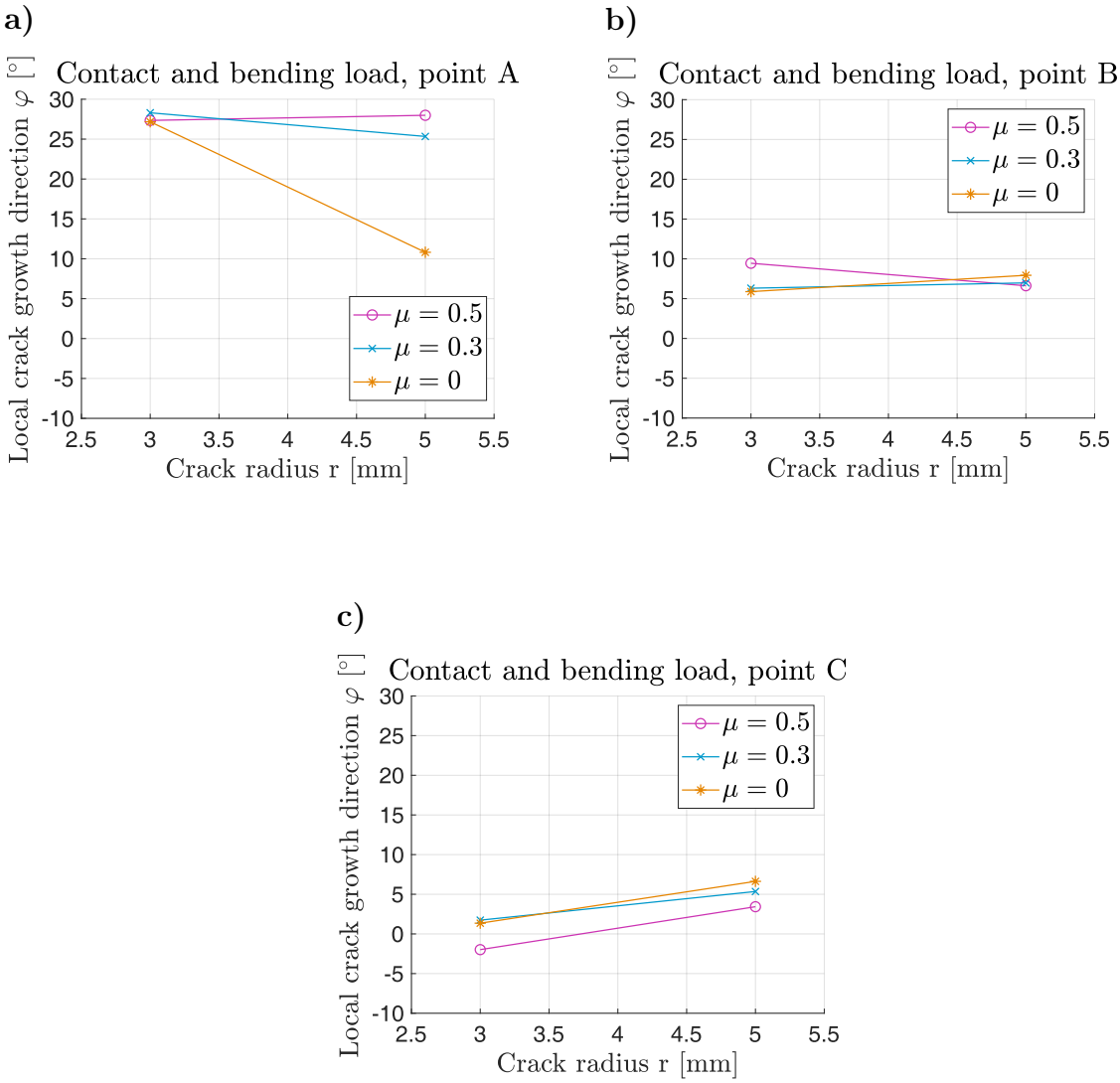


Figure 4.8: Predicted crack growth directions under combined contact and bending load at different evaluation points for varying radii and friction coefficients. (a) Point A. (b) Point B. (c) Point C.

The predicted growth rates in Figure 4.7 shows strong resemblance to the predicted rates for pure contact loading, which in the frictionless case is explained by the low growth rates under pure bending (see Salahi Nezhad et al., 2024). These effects are also observed for the frictional cracks, which aligns with the 2D simulations performed in Salahi Nezhad et al. (2023). Consequently, the growth rate trends are consistent for both load cases. Higher friction coefficients decrease the growth rates for all points and both radii, and increasing the radius to 5 mm amplifies the differences between the friction coefficients for point A and B. More specifically, a friction coefficient of 0.5 results in up to a 49% reduction in growth rate compared to the frictionless crack, while a coefficient of 0.3 gives a reduction of up to 31%. Thus, adding rail bending yields a slightly lower, although still high, influence of friction compared to pure contact loading. This can be expected due to the high negative bending moment in Figure 4.2 (i.e., compressive loading of the crack), which results in lower rates.

The growth directions in Figure 4.8 generally display upward growth. The differences

between friction coefficients are small and within the numerical accuracy level of the employed VCTD criterion, with the exception of point A for $r = 5$ mm, where the influence of friction on promoting upward growth is not numerically small. However, with only two radii studied, as for the case of pure contact load, it is difficult to identify trends in the influence of friction on the growth direction, which thereby remains inconclusive.

In addition, the predicted crack growth rates are compared with field measurements given in (INNOTRACK Consortium, 2009), which shows head check crack growth of 1 mm in depth for 100 Mega Gross Tonnes (MGT) of traffic. Here, MGT to 1 mm crack depth denotes the cumulative gross tonnage that passes the rail before the crack depth reaches 1 mm. The predicted crack growth rates are converted to an equivalent traffic measure assuming a constant crack growth rate such that $\Delta a = \frac{da}{dN}\Delta N$, to get 1 mm crack growth in depth. The evaluated number of cycles to reach a crack depth of 1 mm is then multiplied by the axle load (15 t in this case). For a combined contact and bending load at point A and with $r = 3$ mm, a frictionless crack yields a passing traffic range of 24 MGT $<$ traffic $<$ 37 MGT when considering the upper and lower estimate of the rate. The frictional correspondents have a range of 30 MGT $<$ traffic $<$ 46 MGT and 38 MGT $<$ traffic $<$ 59 MGT for friction coefficients $\mu = 0.3$ and $\mu = 0.5$, respectively. This is equivalent to a traffic increase of about 25% for $\mu = 0.3$ and 58% for $\mu = 0.5$ when comparing to the traffic of a frictionless crack. This emphasizes the importance of incorporating crack face friction for having more realistic and reliable numerical models towards field measurements for optimizing maintenance procedure. As a side note, a similar study has been conducted in Salahi Nezhad et al. (2024), where a different traffic range (47 MGT $<$ traffic $<$ 71 MGT) was reported for a frictionless crack for the same point, radius, and load case. The discrepancy compared to the range obtained in the present study is most likely due to their evaluation of SIFs, which is performed using a displacement-based method proposed in (Andersson et al., 2018) in MATLAB, rather than using built-in features in ABAQUS.

For maintenance planning, it is useful to evaluate the amount of traffic that the rail can endure before cracks reach a certain size. For this, the predicted crack growth rates are employed, assuming that the rail has an initial crack size of $r = 3$ mm. The remaining fatigue life until reaching $r = 5$ mm is calculated by integrating the rates and assuming a linear variation between the two radii. As previously, the passing traffic corresponding to this fatigue life is evaluated by multiplying it by the axle load (15 t in this case). Figure 4.9 shows the results at point A for the case of combined bending and contact load, using the upper estimate of the growth rates. The results clearly show that the amount of traffic increases as the crack face friction increases. More specifically, the amount of traffic is observed to increase by 28% for crack face friction of 0.3 and 72% for crack face friction of 0.5, as compared to the frictionless case. Note that the predictions in Figure 4.9 shows the amount of traffic needed for getting a $r = 5$ mm crack from a $r = 3$ mm crack. In practice, much higher traffic is needed for the stage before this, i.e., from crack initiation to form a $r = 3$ mm crack, which was not in the scope of the current study.

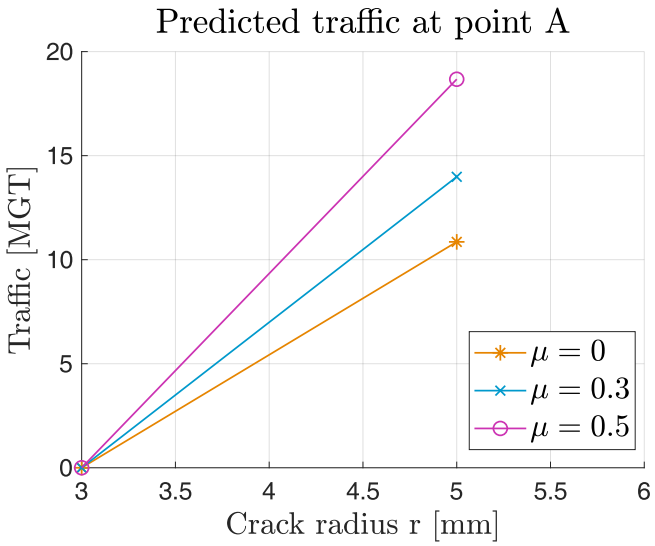


Figure 4.9: Predicted traffic [MGT] evaluated at point A for varying radii and friction coefficients $\mu$.

# 5 Concluding remarks and future work

In this study, an existing numerical framework in 3D for predicting stationary RCF crack growth direction and rate in rails using XFEM (Salahi Nezhad et al., 2024) has been extended to account for the influence of crack face friction. For this, the accuracy and robustness of using XFEM in ABAQUS for stationary frictional cracks in 3D simulations have been assessed by comparing simulated shear stresses at the crack faces using explicit and XFEM crack representation for a rectangular block model. Here, crack face friction was implemented using Coulomb's model. For the rail model, growth rates and directions were evaluated by employing Paris-type equations and an accumulative VCTD criterion, respectively, using SIFs extracted directly from ABAQUS. Results were evaluated for two load scenarios, at three points along the crack front and for two radii.

For implementing a stationary frictional crack in 3D using XFEM in ABAQUS, an approach was used, where crack propagation is technically allowed but suppressed by assigning very high critical values for damage initiation and evolution. The approach was found to successfully enforce crack stationarity in the simulations and to generate a reasonable shear stress response for frictional cases. It was shown in the study that the shear stresses can be approximated with sufficient accuracy by evaluating the stresses in adjacent elements. The predicted shear stress trends agree well with those obtained from explicit crack modeling, although some discrepancies remain in the absolute values. Possible reasons for this include differences in how ABAQUS handles propagating versus stationary cracks, and/or potential reduced accuracy in the element integration for XFEM since the enrichment functions are non-polynomial and discontinuous. Nevertheless, since the overall trends and the influence of crack face friction are consistent, the adopted method is considered sufficiently robust for the qualitative comparison purposes of this study.

Crack face friction was found to reduce crack growth rates for all points, radii, and load cases, with higher friction coefficients leading to greater reductions. The influence of friction also generally becomes more pronounced for larger crack radii, as the increased crack face area promotes more sticking. Consistent trends were observed for both pure contact and combined contact and bending loads, and evaluating the predicted growth rates in terms of traffic (MGT) showed that including crack face friction increases the traffic capacity before reaching critical crack depths. In short, for a combined contact and bending load, having a crack face friction coefficient of 0.3 can reduce the crack growth rates by up to 31% compared to the frictionless case. This number is up to 49% for the case of a crack face friction coefficient of 0.5 in comparison to the frictionless case. As presented in Section 4.3.2, these reductions can lead to a traffic increase of 28% for the crack face friction coefficient of 0.3 and a traffic increase of 72% for the crack face friction coefficient of 0.5 in comparison to the frictionless case, assuming a linear rate variation between crack radii. These results highlight the importance of accounting for crack face friction in order to obtain more realistic predictions and to support efficient maintenance planning. The rate predictions were used to compare with a field measurement in the literature and a reasonably good agreement was there observed. More specifically, the agreement is better when the crack face friction is included, with higher values of predicted traffic.

Growth directions under pure contact load predominantly show upward growth, which also agrees with previous findings in (Salahi Nezhad et al., 2024) for a frictionless crack. However, the differences between friction coefficients are small and within the accuracy limits of the accumulative VCTD criterion. Thus, the influence of crack face friction is judged to be marginal on growth directions. For the combined contact and bending load case, the predicted directions generally display upward growth. Here, the influence of crack face friction is again limited, with only minor deviations observed, such as at point A for $r = 5$ mm. Given that a limited number of cases (only two radii) were analyzed in this study, the overall effect of crack face friction on the crack growth directions remains inconclusive.

The discrepancies observed between XFEM and explicit crack modeling in ABAQUS indicate that further investigation of using XFEM for stationary frictional cracks in 3D simulations would be valuable for more quantitative predictions. One potential approach to this is to examine additional response parameters, such as displacements, to better understand the source of the discrepancies. Another possibility is to investigate alternative approaches for enforcing or implementing stationarity.

For the rail model, the adopted methods for evaluating crack growth rate and direction rely solely on SIFs, which in this study were extracted using a built-in feature in ABAQUS. Exploring alternative evaluation methods, such as the displacement-based approach presented in (Andersson et al., 2018) or any other suitable methods, could potentially improve the accuracy of the predictions. In addition, since only two crack radii are considered in this study, the potential to identify trends is limited. This is especially evident for the crack growth directions, where no clear trends regarding the influence of crack face friction were observed. Including more radii would thus increase the possibility of identifying trends for the growth directions, and could potentially strengthen the observed influence of crack face friction on crack growth rates. Furthermore, adopting a propagating crack instead of being restricted to stationarity, would make more quantitative validations against field data possible. Finally, incorporating more relevant load cases, such as thermal loading, and employing more realistic friction coefficients, reflecting potential lubrication or surface roughness of the crack faces, may improve the accuracy of the numerical framework (by fine-tuning, if needed) and increase the practical relevance of the predictions.

# References


Andersson, R., Kabo, E., & Ekberg, A. (2020). Numerical assessment of the loading of rolling contact fatigue cracks close to rail surface irregularities. *Fatigue & Fracture of Engineering Materials & Structures*, *43*(5), 947–954. https://doi.org/10.1111/ffe.13168

Andersson, R., Larsson, F., & Kabo, E. (2018). Evaluation of stress intensity factors under multiaxial and compressive conditions using low order displacement or stress field fitting. *Engineering Fracture Mechanics*, *189*, 204–220. https://doi.org/10.1016/j.engfracmech.2017.11.015

Belytschko, T., & Black, T. (1999). Elastic crack growth in finite elements with minimal remeshing. *International Journal for Numerical Methods in Engineering*, *45*(5), 601–620. https://doi.org/10.1002/(SICI)1097-0207(19990620)45:5<601::AID-NME598>3.0.CO;2-S

Bergman, M., Annerberg, L., Grönlund, A., Back, S., Nilsson, P., & Fleming, M. S. (2016). *En klimatneutral och hållbar transportsektor* (In Swedish). Svenskt Näringsliv. https://www.svensktnaringsliv.se/sakomraden/hallbarhet-miljo-och-energi/en-klimatneutral-och-hallbar-transportsektor_1109229.html

Dassault Systèmes Simulia Corp. (2023a). *Abaqus (version 2023) [computer software]*. https://www.3ds.com/products-services/simulia/products/abaqus/

Dassault Systèmes Simulia Corp. (2023b). *Abaqus documentation* [SIMULIA User Assistance 2023]. Dassault Systèmes. Retrieved September 22, 2025, from https://help.3ds.com/2023/english/dssimulia_established/

Dassault Systèmes Simulia Corp. (2023c). *Damage evolution* [In *SIMULIA User Assistance 2023* (Abaqus > Abaqus/CAE > Creating and analyzing a model using the Abaqus/CAE modules > The Property module > Defining mechanical material models > Defining damage)]. Retrieved September 22, 2025, from https://help.3ds.com/2023/english/dssimulia_established/SIMACAECAERefMap/simacae-t-prpmechanicaldamageevolution.htm

Dassault Systèmes Simulia Corp. (2023d). *Defining damage* [In *SIMULIA User Assistance 2023* (Abaqus > Abaqus/CAE > Creating and analyzing a model using the Abaqus/CAE modules > The Property module > Defining mechanical material models)]. Retrieved September 22, 2025, from https://help.3ds.com/2023/english/dssimulia_established/SIMACAECAERefMap/simacae-m-PrpMechanicalDamage-sb.htm

Doll, C., Brauer, C., Köhler, J., & Scholten, P. (2020). *Methodology for GHG efficiency of transport modes*. Fraunhofer-Institute for Systems and Innovation Research ISI. https://cedelft.eu/publications/methodology-for-ghg-efficiency-of-transport-modes/

Ekberg, A., & Kabo, E. (2005). Fatigue of railway wheels and rails under rolling contact and thermal loading — an overview. *Wear*, *258*(7-8), 1288–1300. https://doi.org/https://doi.org/10.1016/j.wear.2004.03.039

INNOTRACK Consortium. (2009). *D4.1.4 rail degradation algorithms* (Deliverable report). INNOTRACK, EU FP6 project TIP5-CT-2006-031415. https://www.charmec.chalmers.se/innotrack/deliverables/sp4/d414-f3-rail_degradation_algorithms.pdf

International Energy Agency (IEA). (2019). *The future of rail: Opportunities for energy and the environment*. https://www.iea.org/reports/the-future-of-rail

Khoei, A. R. (2015). Extended finite element formulation. In *Extended finite element method: Theory and applications*. John Wiley Sons. https://doi.org/10.1002/9781118869673

Kuna, M. (2013). *Finite elements in fracture mechanics: Theory, numerics, applications*. Springer.

Moës, N., Dolbow, J., & Belytschko, T. (1999). A finite element method for crack growth without remeshing. *International Journal for Numerical Methods in Engineering*, *46*(1), 131–150. https://doi.org/10.1002/(SICI)1097-0207(19990910)46:1<131::AID-NME726>3.0.CO;2-J

Nielsen, J. C. O., & Igeland, A. (1995). Vertical dynamic interaction between train and track–influence of wheel and track imperfections. *Journal of Sound and Vibration*, *187*(5), 825–839. https://doi.org/10.1006/jsvi.1995.0566

P.B.J. Dollevoet, R. (2010). *Design of an anti head check profile based on stress relief* [Doctoral dissertation, University of Twente]. https://research.utwente.nl/en/publications/design-of-an-anti-head-check-profile-based-on-stress-relief

Salahi Nezhad, M. (2024). *Numerical investigations of rolling contact fatigue crack growth in a rail head* [Doctoral dissertation, Chalmers University of Technology]. https://research.chalmers.se/publication/542086

Salahi Nezhad, M., Floros, D., Larsson, F., Kabo, E., & Ekberg, A. (2022). Numerical predictions of crack growth direction in a railhead under contact, bending and thermal loads. *Engineering Fracture Mechanics*, *261*, 108218. https://doi.org/10.1016/j.engfracmech.2021.108218

Salahi Nezhad, M., Larsson, F., Kabo, E., & Ekberg, A. (2023). Numerical prediction of railhead rolling contact fatigue crack growth. *Wear*, *530-531*, 205003. https://doi.org/https://doi.org/10.1016/j.wear.2023.205003

Salahi Nezhad, M., Larsson, F., Kabo, E., & Ekberg, A. (2024). Finite element analyses of rail head cracks: Predicting direction and rate of rolling contact fatigue crack growth. *Engineering Fracture Mechanics*, *310*, 110503. https://doi.org/https://doi.org/10.1016/j.engfracmech.2024.110503

Statens institut för kommunikationsanalys (SIKA). (2009). *SIKA Basfakta 2008 – Övergripande statistik om transportsektorn* (2009:28) (In Swedish). Statens institut för kommunikationsanalys (SIKA). https://www.researchgate.net/publication/357826998_SIKA_Basfakta_2008_Overgripande_statistik_om_transportsektorn

The MathWorks, Inc. (2022). *Matlab (r2022b) [computer software]*. https://www.mathworks.com/products/matlab.html

V. Krishna, V., Hossein-Nia, S., Casanueva, C., Stichel, S., Trummer, G., & Six, K. (2021). Rail RCF damage quantification and comparison for different damage models. *Railway Engineering Science*, *30*, 23–40. https://doi.org/https://doi.org/10.1007/s40534-021-00253-y

Wriggers, P. (2006). *Computational contact mechanics* (2nd ed.). Springer.

Zerbst, U., Lundén, R., Edel, K.-O., & Smith, R. (2009). Introduction to the damage tolerance behaviour of railway rails – a review. *Engineering Fracture Mechanics*, *76*(16), 2563–2601. https://doi.org/https://doi.org/10.1016/j.engfracmech.2009.09.003

**DEPARTMENT OF INDUSTRIAL AND MATERIALS SCIENCE**
**CHALMERS UNIVERSITY OF TECHNOLOGY**
Gothenburg, Sweden 2025
www.chalmers.se


CHALMERS
UNIVERSITY OF TECHNOLOGY